Crystal Structural Investigation of 2D Materials

A THESIS

Submitted in partial fulfillment of the requirements for the award of the degree of

Master of Science

By

Ashish Meena

(Roll Number: 2303151008)

Department of Physics

Indian Institute of Technology Indore

May 2025

Crystal Structural Investigation of 2D Materials

M.Sc. Thesis

By

Ashish Meena

(Roll Number: 2303151008)

Under the guidance of

Prof. Preeti Bhobe

Department of Physics

Indian Institute of Technology Indore

May 2025

INDIAN INSTITUTE OF TECHNOLOGY INDORE

CANDIDATE'S DECLARATION

I hereby certify that the work which is being presented in the thesis entitled ***Crystal Structural Investigation of 2D Materials*** in the partial fulfillment of the requirements for the award of the degree of **MASTER OF SCIENCE** and submitted in the **DEPARTMENT OF PHYSICS**, Indian Institute of Technology Indore, is an authentic record of my own work carried out during the time period from *August 2023* to *May 2025* under the supervision of *Prof. Preeti Bhobe, Professor, Department of Physics, IIT Indore*.

The matter presented in this thesis has not been submitted by me for the award of any other degree of this or any other institute.

Ashish 20-5-2025

Signature of the student with date

(Ashish Meena)

This is to certify that the above statement made by the candidate is correct to the best of my/our knowledge.

Preeti 20-5-25

Signature of the Supervisor of

M.Sc. thesis #1 (with date)

(Prof. Preeti Bhobe)

Ashish Meena has successfully given his M.Sc. Oral Examination held on **May 2025**.

Dipankar Das

Convener, DPGC

Date: 20-05-25

Acknowledgment

I would like to express my heartfelt gratitude to **Prof. Preeti Bhobe**, my supervisor and faculty adviser, for her continuous support, guidance, and encouragement throughout the course of this project. Her insightful feedback and unwavering mentorship have been instrumental not only in the successful completion of this work but also in shaping my academic journey.

I am also thankful to **IIT Indore** and the **Department of Physics** for providing the Raman spectroscopy facility, which was a key component of the characterization process.

Special thanks to **MEMS** and **Prof. Sen** for extending access to the XRD facility, as well as to the **SIC central facility** for the use of EDX and FE-SEM instruments that played a crucial role in material analysis.

Lastly, I sincerely thank my peers and lab mates for their constant support, valuable discussions, and for creating a collaborative and motivating environment throughout this research.

Abstract

Understanding the crystal structure of two-dimensional (2D) materials is crucial for determining their physical properties and potential applications. This thesis focuses on the structural investigation of Two dimensional Materials like $ZrSe_2$, $TiSe_2$, and $ZrSe_3$, synthesized using the Chemical Vapor Transport (CVT) method. The study employs X-ray Diffraction (XRD) to determine phase purity, lattice parameters, and symmetry, providing insights into stacking configurations and possible distortions. Raman Spectroscopy is used to analyze vibrational modes, which are directly influenced by structural arrangements and layer interactions. Additionally, Field Emission Scanning Electron Microscopy (FESEM) and Energy Dispersive X-ray Spectroscopy (EDX) help examine surface morphology and elemental composition, ensuring proper stoichiometry. The results offer a deeper understanding of how structural variations affect the stability and properties of these materials, contributing to the broader exploration of transition metal chalcogenides for optoelectronic and energy-related applications.

Contents

Chapter 1

Introduction

Two-dimensional (2D) materials have garnered significant attention because of their unique physical and chemical properties, which often differ drastically from those of their bulk counterparts. These materials consist of thin atomic layers that are weakly bonded by van der Waals forces, while the atoms within each layer are strongly connected by interatomic bonds, making it possible to easily peel them into monolayers. A key group within 2D materials is the transition metal chalcogenides (TMCs), which encompass both transition metal dichalcogenides (TMDs) and trichalcogenides. These materials are highly promising for use in various fields such as nanoelectronics, optoelectronics, and energy storage technologies.

Among TMDs, zirconium diselenide ($ZrSe_2$) has attracted growing interest due to its layered hexagonal crystal structure and semiconducting properties. Like its counterparts MoS_2 and WS_2, $ZrSe_2$ exhibits a band gap of approximately 1 eV, making it a potential candidate for next-generation optoelectronic applications. Additionally, the weak interlayer bonding allows for the mechanical exfoliation of monolayers, which could be utilized in flexible and low-power electronic devices. Despite extensive research on other TMDs, $ZrSe_2$ remains relatively unexplored, making it a promising candidate for further study.

In contrast to $ZrSe_2$, zirconium triselenide ($ZrSe_3$) belongs to the trichalcogenide family. Unlike the perfectly layered structure of $ZrSe_2$, $ZrSe_3$ exhibits a quasi-one-dimensional nature with chain-like structural motifs. This distinct crystal structure results in anisotropic electronic and optical properties, which could be advantageous for direction-dependent transport applications and novel low-dimensional device architectures.

Another closely related material is titanium diselenide ($TiSe_2$), which belongs to the same TMD

family as $ZrSe_2$ but exhibits a unique charge density wave (CDW) transition at low temperatures. This structural transition significantly affects its electronic properties, making $TiSe_2$ an exciting material for condensed matter research. Unlike $ZrSe_2$, $TiSe_2$ exhibits a semi-metallic behavior and has been studied extensively for its superconducting and excitonic properties under external perturbations such as pressure and doping.

This study focuses on the synthesis and characterization of $ZrSe_2$, with additional insights into related materials such as $ZrSe_3$ and $TiSe_2$, to understand their structural and electronic properties. Through comprehensive experimental techniques, including X-ray diffraction (XRD) and Raman spectroscopy, this work aims to expand the knowledge of these materials and their potential applications in next-generation technologies.investigation.

1.1 What is Crystal Structure?

The crystal structure of a material describes how its atoms, ions, or molecules are arranged in a regular, repeating pattern within a solid. This systematic organization not only defines the material's spatial arrangement but also plays a crucial role in determining various physical properties, including its electronic behavior, optical features, and mechanical strength.

At the heart of a crystal structure is the **unit cell**—the smallest repeating unit that captures the symmetry and arrangement of the entire crystal. Key aspects of a crystal structure include:

- **Lattice Parameters**: These are the dimensions (edge lengths and angles) of the unit cell, which dictate how the cell repeats in space.
- **Symmetry Elements**: These include rotational axes, mirror planes, and inversion centers, which together define the *space group* of the crystal.
- **Atomic Arrangement**: The specific positioning of atoms or ions within the unit cell, which determines the interactions between them.

Figure 1.1 provides a schematic illustration of a typical crystal lattice. In this figure, you can observe the periodic arrangement of atoms, the concept of the unit cell, and the symmetry that characterizes the overall structure.

Understanding the crystal structure is fundamental, especially in the context of two-dimensional (2D) materials. Variations in structural parameters and symmetry can lead to significant changes in

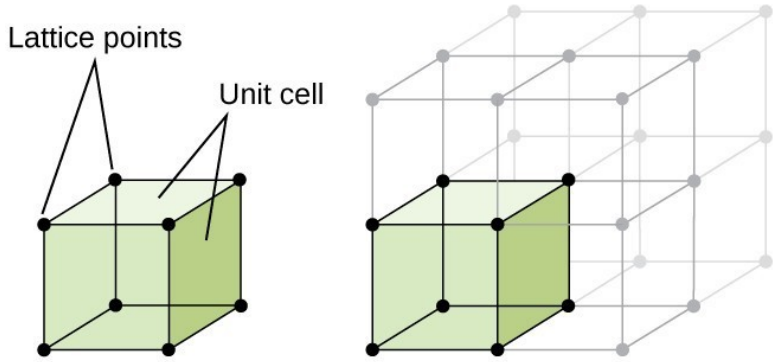

Figure 1.1: Schematic representation of a crystal lattice. The periodic arrangement of atoms, along with the defined unit cell, highlights the structural framework that governs the material's properties.

material behavior, making crystal structural investigation a critical first step in materials research.

1.2 Why is Crystal Structure Crucial in 2D Materials?

Understanding the crystal structure of two-dimensional (2D) materials is fundamental to grasping their unique properties. The arrangement of atoms within these materials dictates a wide range of phenomena that are essential for their application in nanoelectronics, optoelectronics, and beyond. Here, we discuss the key aspects in which crystal structure influences the behavior of 2D materials:

1.2.1 Determinant of Electronic Properties

The electronic band structure is directly influenced by the crystal lattice. For instance, in layered materials such as $ZrSe_2$ and $TiSe_2$, the hexagonal arrangement of atoms and the presence of weak van der Waals interactions facilitate the formation of band gaps that can vary significantly with thickness. This sensitivity is crucial for applications in semiconducting devices, where a tunable band gap is often desired.

1.2.2 Optical and Vibrational Characteristics

The symmetry and periodicity of a crystal lattice define the vibrational (phonon) modes of a material, which in turn determine its Raman and infrared (IR) spectra. In materials like $ZrSe_2$ and $TiSe_2$, the specific arrangement of atoms leads to distinct Raman-active modes that are sensitive to external influences such as strain or temperature. These modes provide insights into interlayer coupling and lattice dynamics, which are critical for understanding light-matter interactions in 2D materials.

1.2.3 Transport Phenomena and Phase Transitions

The crystal structure also plays a pivotal role in governing electronic transport properties and phase transitions. For example, $TiSe_2$ undergoes a charge density wave (CDW) transition that is directly linked to periodic distortions in its lattice. Similarly, the quasi-one-dimensional structure of $ZrSe_3$ results in highly anisotropic transport properties, which can be exploited in designing devices with direction-dependent electrical conductance.

1.2.4 Interlayer Bonding and Structural Stability

In layered 2D materials, the interlayer interactions—typically governed by weak van der Waals forces—are critical for processes such as mechanical exfoliation and the formation of heterostructures. The ease with which layers can be separated or reassembled enables the engineering of novel materials with customized properties. Furthermore, the stability and reactivity of these materials are intrinsically tied to the strength and nature of these interlayer bonds.

1.2.5 Influence of Defects, Disorder, and Strain

Crystal imperfections such as vacancies, interstitials, and stacking faults can significantly modify the electronic and optical properties of 2D materials. For instance, defects in $ZrSe_2$ may lead to unintentional doping, thereby altering its semiconducting behavior. Additionally, external strain can induce changes in the lattice parameters, leading to a shift in the band gap and affecting both electronic and vibrational properties. These effects are key considerations when designing devices based on 2D materials.

1.3 Symmetry and Space Group: The Foundation of Material Properties

The symmetry and space group of a crystal provide a fundamental framework for understanding its physical properties. In 2D materials, these structural descriptors are critical as they dictate not only the atomic arrangement but also influence the electronic band structure, vibrational modes, and optical selection rules. This section explores the multifaceted role that symmetry plays in determining material behavior.

1.3.1 Influence on Electronic Properties

The electronic band structure of a material is inherently linked to its symmetry. High-symmetry crystal lattices tend to produce well-defined electronic bands, while lower symmetry can lead to band splitting and anisotropic conduction paths. For example, materials belonging to a centrosymmetric space group, such as $ZrSe_2$ and $TiSe_2$, often exhibit distinct energy dispersion relations that are sensitive to interlayer interactions. These characteristics not only determine whether the material behaves as a semiconductor, semi-metal, or metal, but also influence phenomena such as charge density wave (CDW) transitions in compounds like $TiSe_2$.

1.3.2 Optical Selection Rules and Anisotropy

Optical properties, including absorption and photoluminescence, are also directly affected by the symmetry of the crystal. The optical selection rules, which govern electronic transitions, are derived from the underlying symmetry of the material. In lower-symmetry systems or in materials with anisotropic crystal structures (e.g., $ZrSe_3$ with its quasi-one-dimensional characteristics), light absorption and emission become directionally dependent, opening up opportunities for polarization-sensitive devices.

1.3.3 Role in Defect Formation and Strain Effects

Symmetry considerations extend to the formation and behavior of defects. In high-symmetry lattices, defects such as vacancies and interstitials can lead to predictable modifications in the electronic structure, whereas in lower-symmetry materials, defect states may introduce localized electronic levels that significantly alter conduction properties. Additionally, strain engineering, which deliberately distorts the crystal lattice, can break or modify the inherent symmetry, thereby tuning the band structure and enhancing certain optical or electronic responses.

In summary, the crystal symmetry and space group serve as the foundational pillars that define a material's intrinsic properties. A comprehensive understanding of these factors is essential for tailoring 2D materials for specific applications in nanoelectronics, optoelectronics, and quantum technologies.

1.3.4 Determination of Vibrational and Optical Modes

The space group of a material dictates the allowed vibrational modes, which are observable in Raman and infrared (IR) spectroscopy. The symmetry elements present in the crystal structure determine which phonon modes are Raman-active or IR-active. In 2D materials, changes in symmetry—for instance, when transitioning from bulk to monolayer—can lead to significant shifts in these vibrational modes. Such shifts provide insights into interlayer coupling and can be used to monitor structural integrity and external perturbations like strain.

1.4 Vibrational and Optical Modes in 2D Materials

Vibrational and optical modes in 2D materials, especially in transition metal dichalcogenides (TMDs), are crucial for understanding their electronic, optical, and thermal properties. These materials typically crystallize in hexagonal structures, leading to specific vibrational modes that can be observed through techniques like Raman and infrared (IR) spectroscopy.

In general, the lattice vibrations in a crystal can be classified into two main types:

- **Acoustic Modes:** These are low-frequency modes in which atoms move in a coordinated fashion, similar to the propagation of sound waves. In a monolayer 2D material with N atoms per unit cell, three acoustic modes are always present: one longitudinal acoustic (LA) mode and two transverse acoustic (TA) modes.

- **Optical Modes:** These modes occur when the atoms in the unit cell move out of sync with each other. They are further categorized into longitudinal optical (LO) and transverse optical (TO) modes.

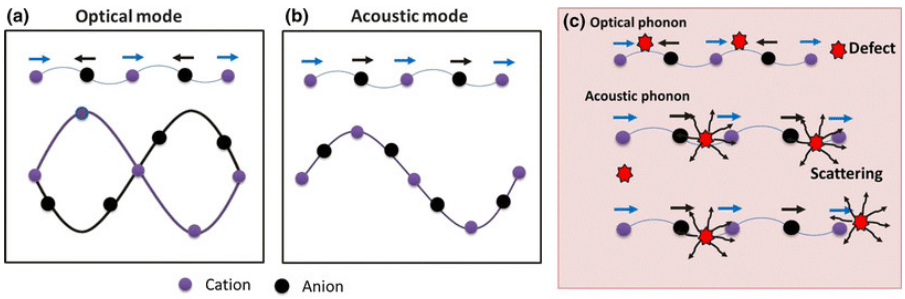

Figure 1.2: Schematic illustration showing: (a) an optical phonon mode, (b) an acoustic phonon mode, both with their corresponding waveforms in a crystal lattice, and (c) the scattering of phonons caused by defects within the crystal structure.

The vibrational modes at the center of the Brillouin zone (Γ point) can be described using group theory. In centrosymmetric materials like 1T-$ZrSe_2$, the vibrational modes can be classified as:

$$\Gamma_{vib} = A_{1g} + E_g + 2A_{2u} + 2E_u \tag{1.1}$$

where:

- A_{1g} and E_g are Raman active (visible in Raman spectra),
- A_{2u} and E_u are IR active (visible in IR spectra),
- A_{1g} is a symmetric out-of-plane vibration,
- E_g corresponds to in-plane vibrations.

The energy of these vibrational modes can be approximated using the harmonic oscillator model:

$$E = \hbar\omega \left(n + \frac{1}{2} \right) \tag{1.2}$$

where:

- $\hbar$ is the reduced Planck's constant,
- ω is the angular frequency of vibration,
- n is the vibrational quantum number.

These vibrational properties are essential for understanding the optical responses, thermal conductivity, and electron-phonon interactions in 2D TMDs.

Chapter 2

Experimental Methods

2.1 Synthesis Methods

2.1.1 Chemical Vapor Transport (CVT) Method

Chemical Vapor Transport (CVT) is a commonly employed technique for growing high-quality single crystals of materials such as transition metal dichalcogenides (TMDs), certain oxides, and intermetallic compounds. The method works by transporting a solid in its vapor phase with the help of a transport agent, all within a controlled temperature gradient. This setup allows for fine control over how the crystals form and grow, which makes CVT a reliable method for preparing well-structured single crystals for both experimental studies and technological use.

Principle of CVT

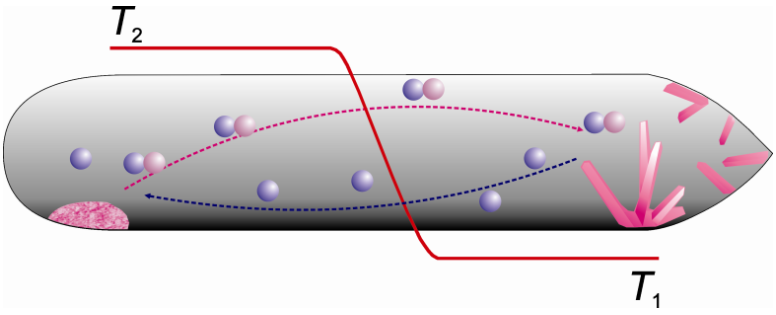

Figure 2.1: Schematic illustration of the Chemical Vapor Transport (CVT) process, showing the crystallization of solids occurring along a controlled temperature gradient.

In the CVT process, a source material (precursor) is placed in a sealed ampoule along with a transport agent, such as iodine (I_2), bromine (Br_2), or chlorine (Cl_2). The ampoule is then evacuated

and sealed under vacuum to prevent contamination. When subjected to a temperature gradient, the source material reacts with the transport agent to form volatile species in the hot zone. These gaseous intermediates migrate to the colder zone, where they decompose, leading to the deposition of single crystals.

The general transport reaction can be represented as:

$$MX_2(s) + X_2(g) \rightleftharpoons MX_n(g) + X_m(g) \tag{2.1}$$

$$MX_n(g) + X_m(g) \rightarrow MX_2(s) + X_2(g) \tag{2.2}$$

where MX_2 represents the source material (e.g., $ZrSe_2$), X_2 is the transport agent (e.g., I_2), and MX_n and X_m are the volatile intermediates formed during transport.

The Chemical Vapor Transport (CVT) method is highly significant due to its ability to produce high-purity crystals, as the transport process helps eliminate impurities, resulting in single crystals suitable for electronic and optical applications. It also allows precise control over crystal size and morphology through careful adjustment of the temperature gradient and transport agent concentration. Moreover, the method is known for its reproducibility, offering a reliable and scalable approach for growing crystals with consistent properties. Another key advantage is its versatility, as it can be applied to synthesize a wide range of materials, including semiconductors, superconductors, and layered compounds.

Precautions in CVT

Despite its advantages, the Chemical Vapor Transport (CVT) method requires careful handling due to several challenges. Proper sealing of the ampoule is crucial, as it must be evacuated and sealed correctly to avoid oxidation or unwanted side reactions. The selection of the transport agent also demands caution; halogens such as iodine (I_2) and bromine (Br_2) are highly reactive and must be handled with care. Temperature control plays a vital role—excessive temperatures can lead to decomposition, while an improper temperature gradient may hinder crystal growth. Additionally, the handling of toxic vapors produced during the process necessitates the use of a fume hood to ensure laboratory safety. There is also a risk of ampoule explosion due to rapid heating or increased internal pressure, which can be mitigated by gradual heating and careful pressure monitoring. Chemical Vapor

Transport is an essential technique for synthesizing high-quality crystals with well-controlled structures. By optimizing reaction conditions and following safety precautions, researchers can achieve reproducible and scalable growth of materials for advanced applications in condensed matter physics, optoelectronics, and nanotechnology.

2.1.2 Solid-State Synthesis Method

The solid-state synthesis method, also known as the ceramic method, is one of the most widely used techniques for synthesizing inorganic compounds, including oxides, sulfides, and intermetallic materials. This method is based on the diffusion of reactant species in the solid state at high temperatures, leading to the formation of a stable crystalline phase.

Solid-state synthesis is a widely used technique that involves several fundamental steps. It begins with the selection of high-purity solid precursors, such as metal oxides, carbonates, or sulfides, chosen based on their reactivity and stoichiometry. These precursors are then accurately weighed and thoroughly mixed to ensure a homogeneous distribution of components, using tools such as a mortar and pestle, ball mill, or planetary mill. In some cases, the resulting powder is pelletized to improve contact between the reactants. The mixed materials are then subjected to calcination and sintering, processes that involve heating at elevated temperatures to facilitate diffusion and reaction between the solid particles. After completion of the reaction, the product is slowly cooled to room temperature and ground into a fine powder to achieve uniform phase distribution. Finally, the synthesized material is characterized using techniques like X-ray diffraction (XRD), Raman spectroscopy, and electron microscopy to confirm its structural and morphological features.

The underlying reaction mechanism in solid-state synthesis is primarily governed by nucleation and growth, where small nuclei form and grow into larger crystalline domains. The overall process is diffusion-controlled, relying on the movement of atoms through the solid matrix—a behavior influenced by factors such as temperature, particle size, and the mobility of the reactants. Reactions mainly occur at the interface between contacting solid particles, which facilitates phase transformation and crystallization.

Solid-state synthesis offers several advantages, including the production of high-purity crystalline materials, simplicity, cost-effectiveness, and suitability for large-scale fabrication. However, the method also presents some limitations. It generally requires high temperatures, which leads to increased energy consumption. The reactions proceed slowly due to diffusion constraints, and it is

often challenging to precisely control the particle size and morphology of the final product.

2.2 Experimantal techniques

2.2.1 Raman Spectroscopy

Raman spectroscopy is a widely used technique for examining the vibrational and low-frequency excitations in solids and molecules. The method is named after C.V. Raman, who first observed the phenomenon in 1928. It works by directing monochromatic light—usually from a laser—onto a sample, where a small portion of the light undergoes inelastic scattering due to interactions with vibrational modes (phonons) in the material. This scattering causes a shift in the energy of the photons, producing a spectrum that acts like a unique signature of the material. Through this, Raman spectroscopy allows for the identification and structural analysis of various compounds. [**?**].

Fundamental Principles

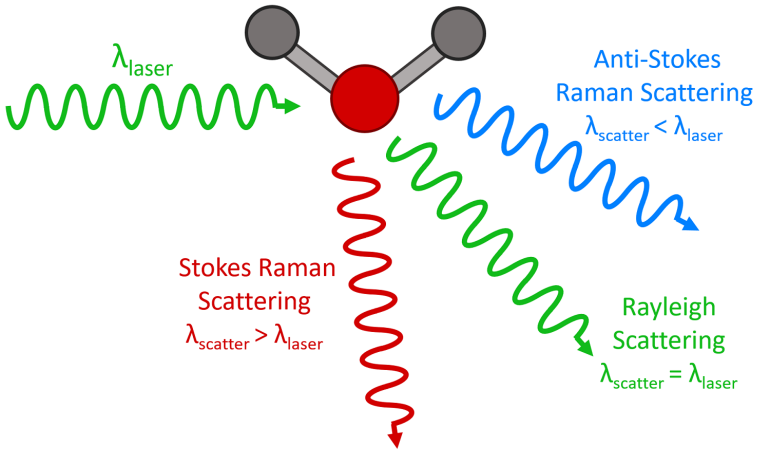

Figure 2.2: Illustration of the three main scattering processes—Rayleigh, Stokes, and Anti-Stokes—that occur when light interacts with a molecule [8].

The working principle of Raman spectroscopy is based on how photons interact with molecular vibrations. When a beam of light strikes a material, the majority of photons are scattered without any change in energy—a process known as Rayleigh scattering. However, a small portion of the light experiences a change in energy due to inelastic scattering, known as Raman scattering. In this case, the energy difference between the incident and scattered photons reflects the vibrational transitions within the material. These energy shifts offer valuable insights into the vibrational states and structural properties of molecules [9].

Classical and Quantum Mechanical Interpretations

From a classical perspective, Raman scattering can be understood through the concept of molecular polarizability. When an external electric field, such as that from incident light, interacts with a molecule, it induces a dipole moment proportional to the field strength and the molecule's polarizability. If the polarizability changes during molecular vibrations, the induced dipole oscillates not only at the frequency of the incident light but also at frequencies corresponding to the sum and difference of the incident light and vibrational frequencies. This leads to the appearance of Stokes and anti-Stokes lines in the Raman spectrum [7].

Classical Interpretation

From a classical perspective, Raman scattering can be understood as the result of the interaction between the electric field of the incoming light and the dipole moment that is temporarily induced in the molecule. This induced dipole moment μ is expressed as:

$$\mu = \alpha E_0 \cos(\omega t) \tag{2.3}$$

Here, α represents the molecular polarizability, E_0 is the amplitude of the electric field, and ω is the frequency of the incident light. When the polarizability depends on the vibrational coordinate Q, it becomes a time-dependent quantity, reflecting the vibrational motion of the molecule.

$$\alpha = \alpha_0 + \left(\frac{\partial \alpha}{\partial Q}\right)_0 Q_0 \cos(\omega_v t) \tag{2.4}$$

Multiplying these gives terms oscillating at frequencies ω, $\omega - \omega_v$ (Stokes), and $\omega + \omega_v$ (anti-Stokes), thus explaining the origin of Raman scattering components.

Quantum Mechanical Interpretation

In quantum mechanics, the Raman process involves a two-photon event. The molecule absorbs a photon of energy $h\nu_i$, transitions to a virtual state, and then relaxes by emitting a photon of different energy $h\nu_s$. The energy difference corresponds to a vibrational transition:

$$\Delta E = h\nu_i - h\nu_s = \Delta E_{vib} \tag{2.5}$$

If $\nu_i > \nu_s$, Stokes scattering occurs, and if $\nu_i < \nu_s$, anti-Stokes scattering is observed.

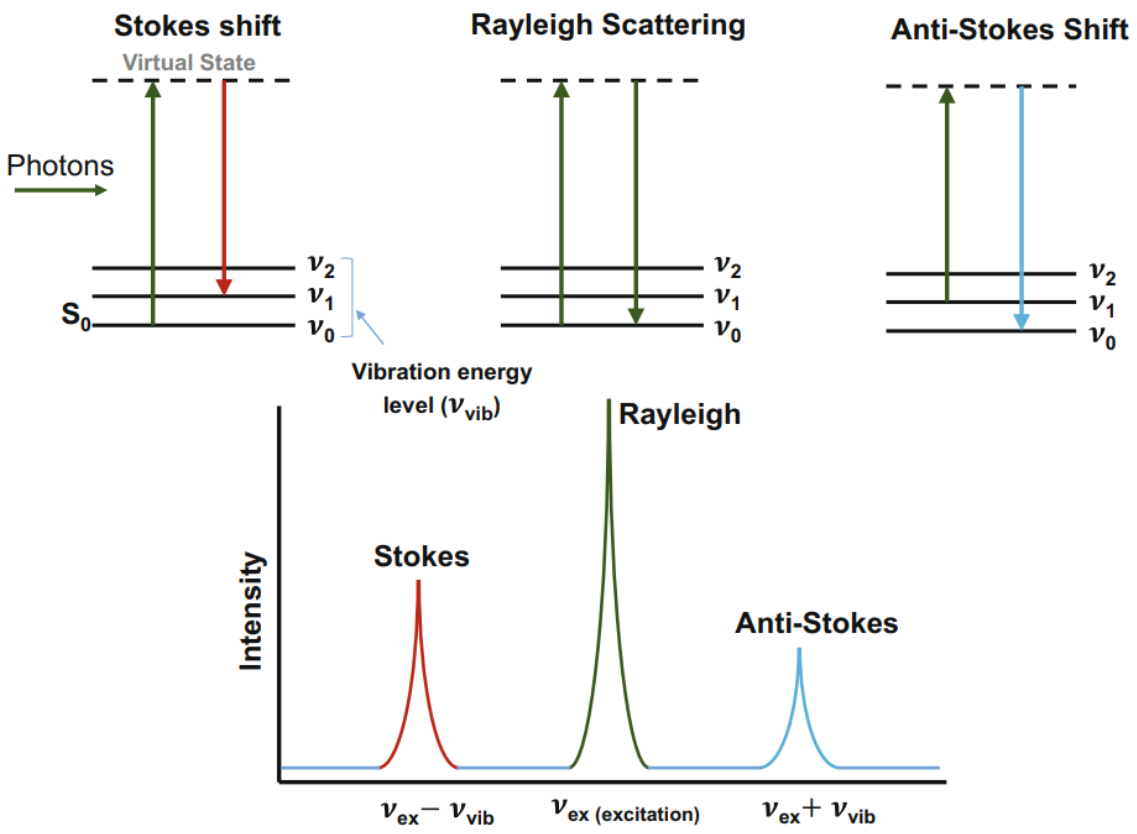

Figure 2.3: Quantum mechanical energy level diagram showing virtual transitions in Raman scattering.

Raman Shift Equation

The Raman shift ($\Delta\tilde{\nu}$) is typically expressed in wavenumbers (cm^{-1}) and is calculated using the equation:

$$\Delta\tilde{\nu} = \left(\frac{1}{\lambda_0} - \frac{1}{\lambda_1}\right) \times 10^7 \tag{2.6}$$

where λ_0 is the wavelength of the incident light, and λ_1 is the wavelength of the scattered light, both in nanometers. This equation allows for the determination of the energy difference between the incident and scattered photons, corresponding to specific molecular vibrations [9].

Raman-Active Modes

Not all vibrational modes are Raman-active. For a vibrational mode to be Raman-active, it must involve a change in the polarizability of the molecule during the vibration. This criterion is expressed mathematically as:

$$\left(\frac{\partial\alpha}{\partial Q}\right) \neq 0 \tag{2.7}$$

where α is the polarizability and Q is the normal coordinate of the vibration. This selection rule implies that only those vibrational modes that cause a change in the polarizability tensor of the molecule will be observed in the Raman spectrum [8].

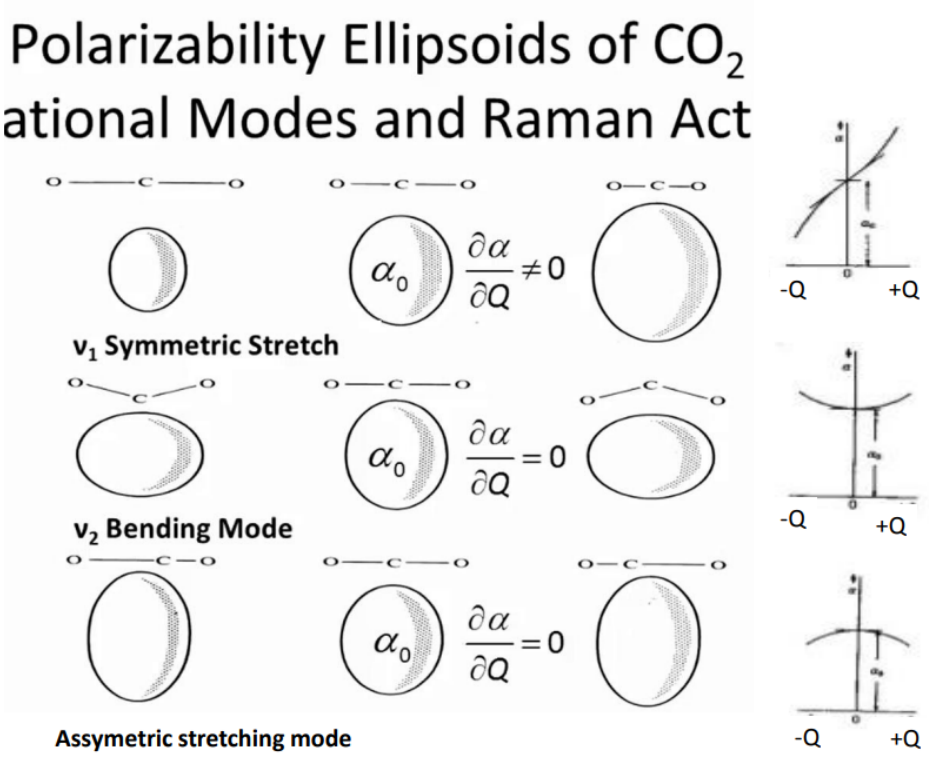

Figure 2.4: Polarizability ellipsoids of CO_2 for symmetric stretching, bending, and asymmetric stretching modes.

Figure 2.4 illustrates the polarizability ellipsoids of CO_2 during different vibrational modes. The symmetric stretching mode (v_1) shows a change in polarizability ($\frac{\partial \alpha}{\partial Q} \neq 0$) and is Raman-active. In contrast, the bending mode (v_2) and asymmetric stretching mode do not induce a change in polarizability ($\frac{\partial \alpha}{\partial Q} = 0$), making them Raman-inactive. Thus, only vibrations that alter the molecular polarizability are observable in Raman spectra.

This visual representation supports the mutual exclusion principle: in centrosymmetric molecules like CO_2, vibrational modes are either Raman-active or infrared-active, but not both. The symmetric stretch alters the polarizability and appears in Raman spectra, while the asymmetric stretch and bending modes primarily alter dipole moment and are thus IR-active but Raman-inactive. [10].

Applications and Instrumentation

Raman spectroscopy is particularly advantageous for studying materials in various states—solid, liquid, or gas—without extensive sample preparation. It is especially valuable in characterizing crystalline materials, polymers, and biological samples. In solid-state physics, Raman spectroscopy aids

in identifying phonon modes, assessing crystal orientation, and detecting phase transitions. The technique's sensitivity to molecular vibrations makes it complementary to IR spectroscopy, providing a more comprehensive understanding of molecular structures [9].

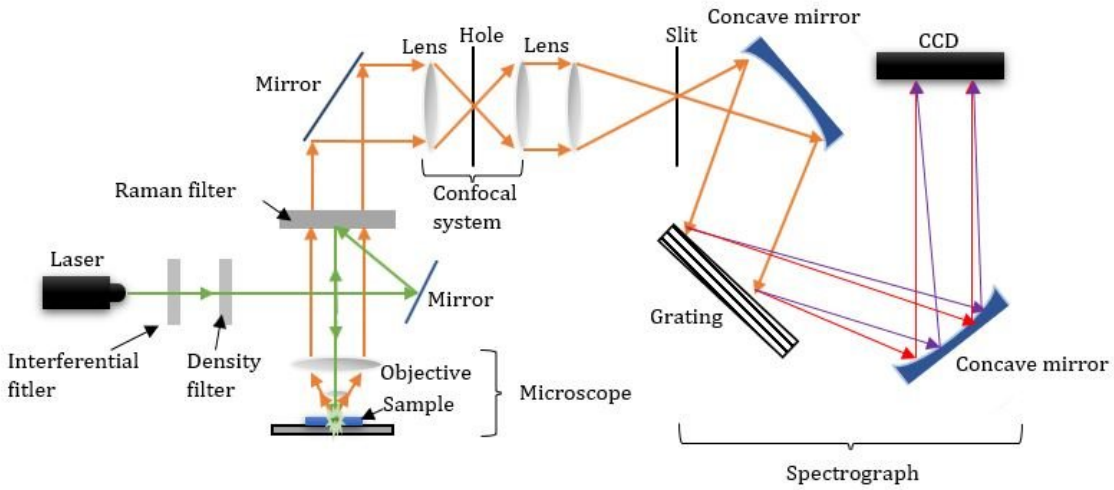

Figure 2.5: Schematic of a micro-Raman spectrometer where illumination and collection are performed through a microscope objective [8].

Advancements in instrumentation, such as the development of laser sources and sensitive detectors, have significantly enhanced the capabilities of Raman spectroscopy. Modern Raman spectrometers can rapidly acquire high-resolution spectra, facilitating real-time analysis and expanding the technique's applications across various scientific disciplines [9].

2.2.2 X-ray Diffraction (XRD)

X-ray diffraction (XRD) stands as a fundamental tool in the study of crystalline materials. Widely utilized across materials science and crystallography, it facilitates insights into various structural aspects such as phase identification, lattice constants, crystallite dimensions, and internal strains. This technique operates on the principle that incident X-rays interact with the periodic atomic layers within a crystal, producing diffraction patterns that reveal vital information about the material's internal arrangement. [17] [5]

Generation of X-rays

X-rays used for diffraction purposes are usually produced within an X-ray tube. In this setup, electrons are emitted from a heated cathode and then accelerated toward a metal target (anode) under

a high-voltage potential. When these high-energy electrons collide with the target, they decelerate rapidly and interact with the atoms of the target material. This interaction gives rise to X-rays through two main processes: bremsstrahlung (braking radiation) and characteristic radiation.

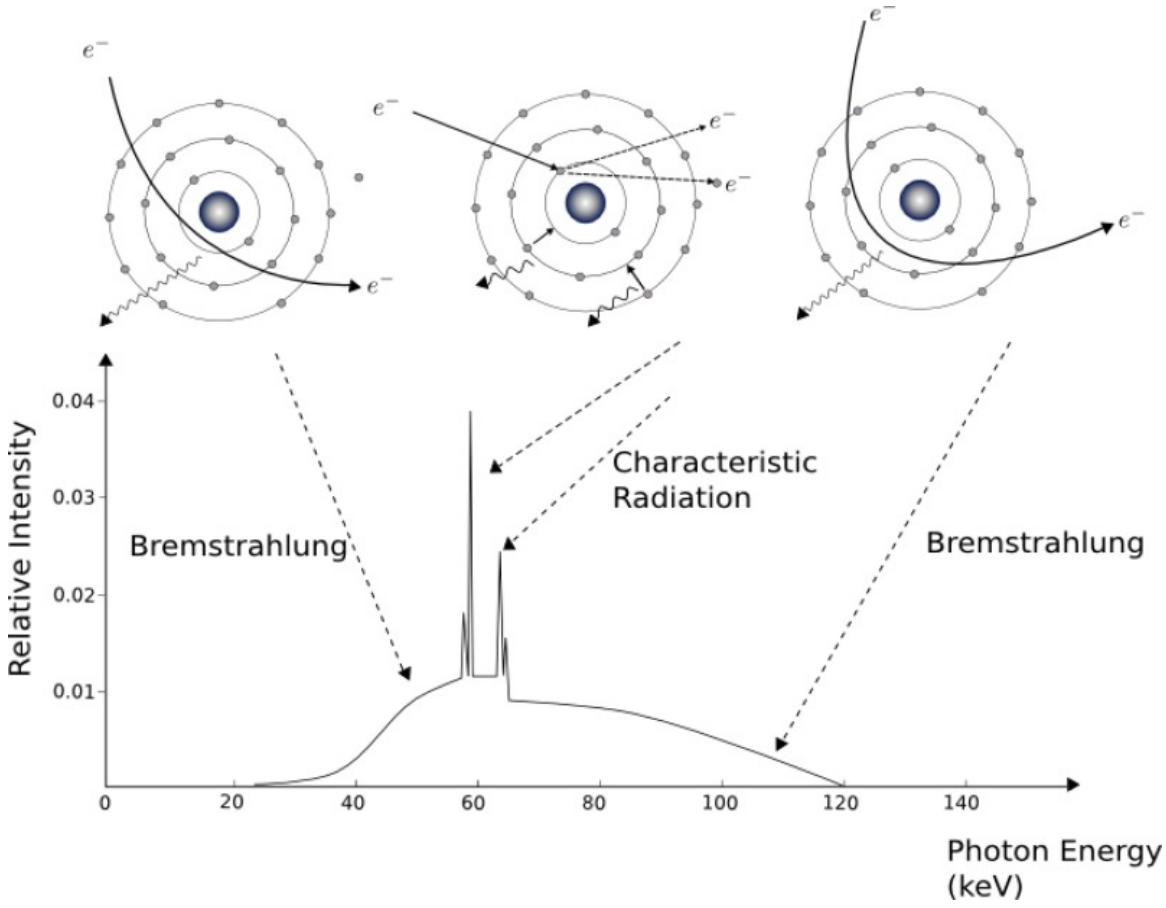

Figure 2.6: X-ray spectrum produced by a tungsten target in an X-ray tube. The peaks correspond to characteristic radiation, while the continuous portion of the spectrum represents bremsstrahlung radiation [17].

Bremsstrahlung Radiation ("Braking Radiation")

Bremsstrahlung, a term derived from German meaning "braking radiation," refers to the X-ray emission that occurs when fast-moving electrons are decelerated or deflected by the electrostatic field of nuclei in the target material. This process does not involve discrete energy transitions, and hence it produces a continuous spectrum of X-ray energies. The emitted photons can span a broad energy range, starting from near zero up to the maximum energy corresponding to the initial kinetic energy of the incident electrons.

Characteristic X-ray Emission

In contrast to bremsstrahlung, characteristic radiation arises from specific electronic transitions within atoms of the anode material. When incoming high-energy electrons have sufficient energy to dislodge electrons from inner atomic shells (typically the K-shell), the resulting vacancy is filled by an electron from a higher energy level, such as the L or M shell. This transition releases energy in the form of an X-ray photon with a well-defined energy unique to the element in question. As an example, copper (Cu) emits a strong Kα line at a wavelength of 1.5406 Å, which is widely employed in standard X-ray diffraction (XRD) instrumentation due to its favorable properties.

X-rays are ideal for probing atomic-scale structures because their wavelengths (typically 0.5–2 Å) are on the order of interatomic distances in crystals. This allows them to be diffracted by the periodic lattice planes according to the laws of wave interference, making them effective tools for revealing atomic arrangements in solids.

Principle of X-ray Diffraction

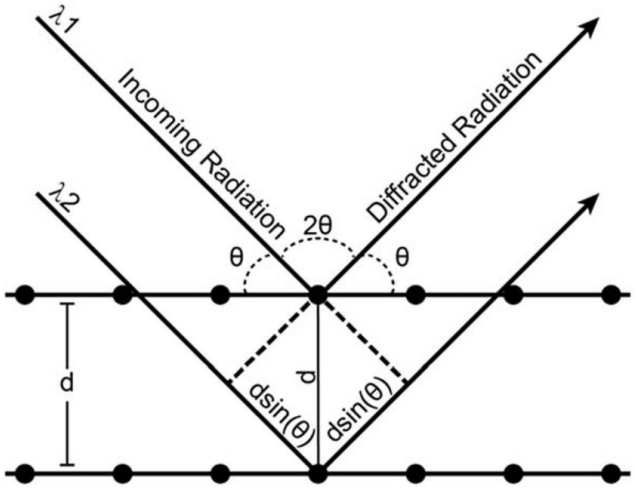

Figure 2.7: Bragg diffraction from parallel atomic planes in a crystal. [19]

When X-rays encounter a crystalline solid, they are scattered by the periodic arrangement of atoms within the crystal lattice. Under certain geometric conditions, these scattered waves can reinforce each other through constructive interference, producing distinct diffracted beams. This behavior is described mathematically by Bragg's law:

$$n\lambda = 2d\sin\theta$$

Here, n is an integer corresponding to the order of diffraction, λ denotes the wavelength of the incident X-rays, d is the distance between adjacent atomic planes, and θ represents the angle at which the incident beam strikes these planes. Bragg's law provides a foundational link between the structural arrangement within the crystal and the conditions required for diffraction to occur.

As the sample is rotated across a range of 2θ angles, various orientations of the crystallites are encountered—especially in powdered samples where the orientation is random—ensuring that all possible diffraction conditions are satisfied. The resulting diffraction pattern, when converted to interplanar spacings (d-values), acts as a fingerprint for identifying crystalline phases. Each material exhibits a unique set of d-spacings, which can be matched against standard databases for identification. [18]

A typical X-ray diffractometer is composed of three essential components: the X-ray source, a stage to hold the sample, and a detector to capture the diffracted beams .

X-ray Diffraction Geometry (Bragg–Brentano Configuration)

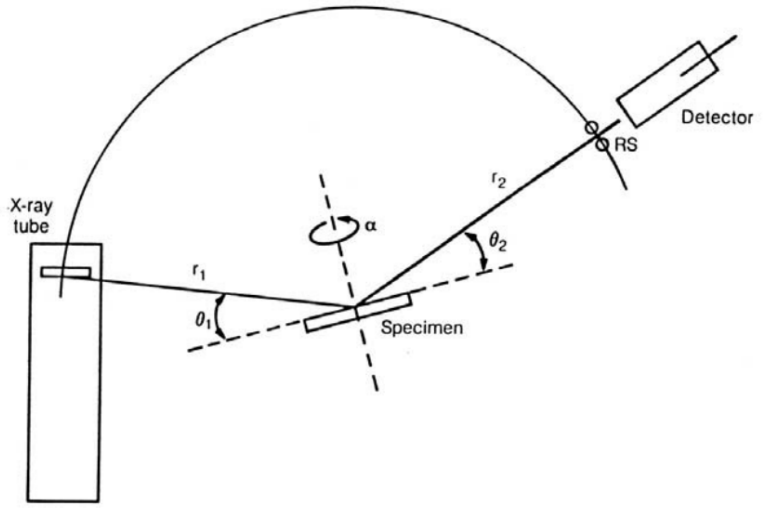

Type	Tube	Specimen	Receiving Slit	r_1	r_2
Bragg-Brentano $\theta:2\theta$	Fixed	Varies as θ*	Varies as 2θ	Fixed	$=r_1$
Bragg-Brentano $\theta:\theta$	Varies as θ	Fixed *	Varies as θ	Fixed	$=r_1$

Figure 2.8: Schematic illustration of the Bragg–Brentano XRD geometry with corresponding motion configurations.

The Bragg–Brentano geometry is one of the most widely used configurations for X-ray powder diffraction, known for its symmetric alignment and ease of operation. In this setup, the X-ray tube emits a beam directed toward the surface of the specimen placed at the center of a goniometric circle.

The incident beam forms an angle θ with the sample surface.

The detector, positioned on the same circular path but on the opposite side of the sample, is arranged to detect the diffracted X-rays at an angle 2θ from the incident beam direction. As the measurement proceeds, the specimen may either remain stationary or rotate depending on the mode of operation, while the detector moves accordingly to maintain the proper diffraction condition as dictated by Bragg's law.

For typical θ-2θ scans, the sample rotates by an angle θ while the detector moves by 2θ, maintaining the condition for constructive interference from crystal planes. This scanning method ensures that all orientations of crystallites in a randomly oriented powder can fulfill Bragg's condition, making it ideal for phase identification and structural analysis.

The design ensures that the paths of the incident and diffracted beams are symmetric with respect to the sample surface, and the distances from the sample to the source and to the detector are often kept equal to preserve this symmetry. The rotation axis of the sample, typically denoted by α, may also be adjusted to accommodate different types of specimens or to enhance alignment precision.

This geometry provides accurate diffraction angles and is particularly useful for analyzing powdered or polycrystalline materials, where random orientation allows access to multiple lattice planes during scanning. [18]

Quantitative Structural Analysis via Rietveld Refinement

For a more rigorous interpretation of diffraction data, the Rietveld refinement method is often employed. Unlike basic peak-based analysis, this approach fits the entire diffraction profile using a structural model grounded in crystallography. The refinement process iteratively modifies parameters such as lattice metrics, atomic positions, and site occupancies to achieve the closest match between simulated and experimental patterns. It also incorporates corrections for instrumental factors including background noise, peak asymmetry, and preferred orientation. The fidelity of the refinement is assessed through statistical measures such as the weighted-profile R-factor (R_{wp}), which serves as a quantitative index of model accuracy [18, 19].

Applications in 2D Layered Materials

In the case of layered TMDs and similar 2D structures, XRD serves as a diagnostic method to examine phase integrity and detect alterations brought about during fabrication or post-processing steps. It

helps confirm crystalline quality and assess texture through peak sharpness and intensity. A prevalent feature in such materials is the dominance of (00l) reflections, indicative of a high degree of planar alignment due to layer-stacking anisotropy. Additionally, any observed shifts in these reflections can be correlated with modifications in interplanar distances, often attributed to intercalation, exfoliation, or elemental substitution. Through such measurements, one can monitor doping effects and lattice distortions, aiding in the fine-tuning of functional attributes in 2D materials [5, 18].

2.2.3 Surface Imaging and Elemental Profiling Using FE-SEM and EDX

To investigate the fine surface features and microstructure of materials at the nanoscale, a field emission scanning electron microscope (FE-SEM) was employed. This technique enables high-resolution visualization of surface morphology and texture. For compositional insights, the system was coupled with energy-dispersive X-ray spectroscopy (EDX), which facilitates rapid identification of elemental constituents within the sample. Together, FE-SEM and EDX form a robust analytical combination, offering both structural and chemical characterization in a single experimental setup. This integrated approach is particularly valuable for studying low-dimensional materials, such as transition metal dichalcogenides (TMDs), where both morphology and composition play critical roles in determining material properties. [20, 21]

Principle of FESEM

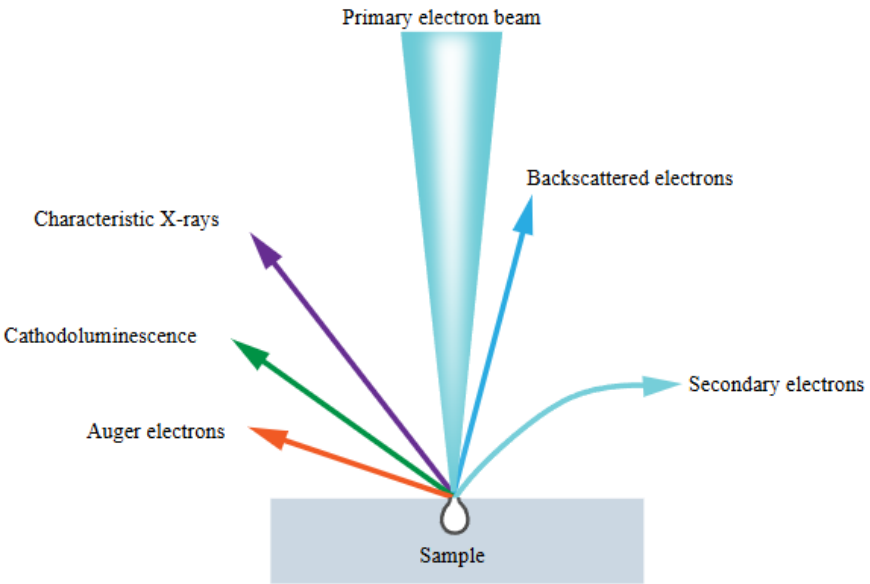

Figure 2.9: Schematic of a FESEM system showing electron beam-sample interaction.

FESEM is an advanced imaging technique that involves directing a finely focused beam of electrons across the surface of a specimen. The underlying principle centers on capturing the various signals emitted as the high-energy electron beam interacts with the sample, thereby enabling the construction of detailed, high-resolution images. Unlike traditional scanning electron microscopy, FE-SEM employs a field emission gun (FEG) as its electron source. This gun utilizes quantum tunneling to emit electrons under a strong electric field, producing a highly coherent and narrow electron beam. The resulting improvement in spatial resolution and the minimization of electron-induced damage make FESEM particularly advantageous for studying nanoscale structures and sensitive materials.

During the interaction between the incident electron beam and the specimen, multiple types of signals are produced. Among them, secondary electrons primarily contribute to imaging by revealing fine surface features and topographical details. Backscattered electrons, on the other hand, are sensitive to the atomic number of the material and are useful for compositional contrast. Additionally, the generation of characteristic X-rays allows for qualitative and quantitative elemental analysis, which is typically performed using EDX [20, 21].

Resolution and Imaging Capabilities

FESEM can achieve resolutions below 1 nm due to its high-brightness electron source. The technique allows imaging of nanostructures, surface grains, voids, edges, and layered morphology with excellent clarity. Image contrast depends on factors such as surface geometry, composition, and crystallinity.

Elemental Analysis via Energy-Dispersive X-ray Spectroscopy (EDX)

Energy-Dispersive X-ray Spectroscopy (EDX) is often integrated with electron microscopy platforms such as SEM and FE-SEM to assess the elemental composition of materials. The method operates on the principle that when the incident electron beam interacts with the sample, it can dislodge electrons from the inner shells of atoms. This triggers a relaxation process in which electrons from higher energy levels transition downward, releasing X-ray photons with energies that are uniquely characteristic of the elements present.

These emitted X-rays are detected and translated into a spectrum showing intensity versus photon energy. The resulting peaks in the spectrum are indicative of specific elements, making it possible to perform both qualitative identification and approximate quantitative analysis of the sample's

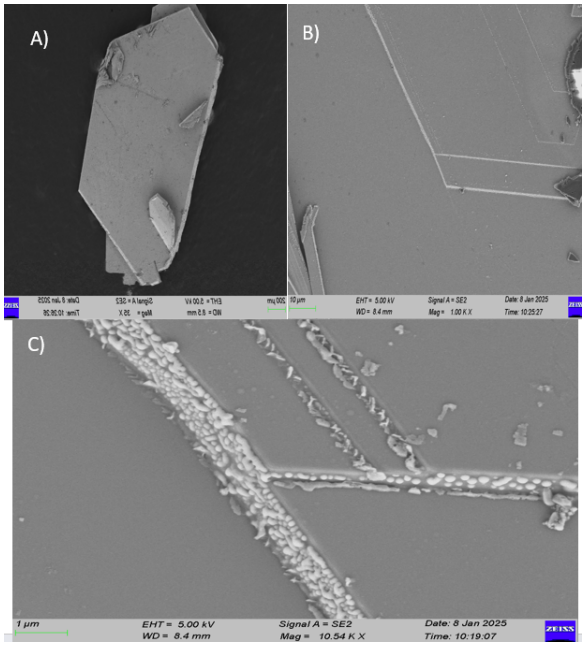

Figure 2.10: Representative FESEM image of a 2D material surface showing layered morphology.

composition. [20, 21]

Applications in TMDs and Nanomaterials

Field Emission Scanning Electron Microscopy (FESEM), when coupled with Energy Dispersive X-ray Spectroscopy (EDX), serves as a powerful diagnostic approach for examining the microstructural and elemental characteristics of two-dimensional materials and nanostructured systems. This combination is particularly beneficial for observing the surface topography of thin flakes, as well as estimating their thickness with high precision. Moreover, it facilitates the identification of structural imperfections such as folds, ruptures, or uneven edges, which are critical for understanding the physical integrity of nanoscale materials. In addition to morphological inspection, EDX analysis enables elemental verification, assisting in the detection of foreign atoms or compositional irregularities that may result from synthesis processes. These techniques also prove valuable in drawing correlations between growth conditions and the resulting structural attributes, thus offering insights that can guide the optimization of material synthesis and processing strategies.

2.2.4 Electrical Resistivity Measurements

Electrical resistivity measurements as a function of temperature are fundamental for probing charge transport mechanisms in materials. This is particularly important for low-dimensional systems such as two-dimensional (2D) materials, where quantum confinement and surface effects can significantly

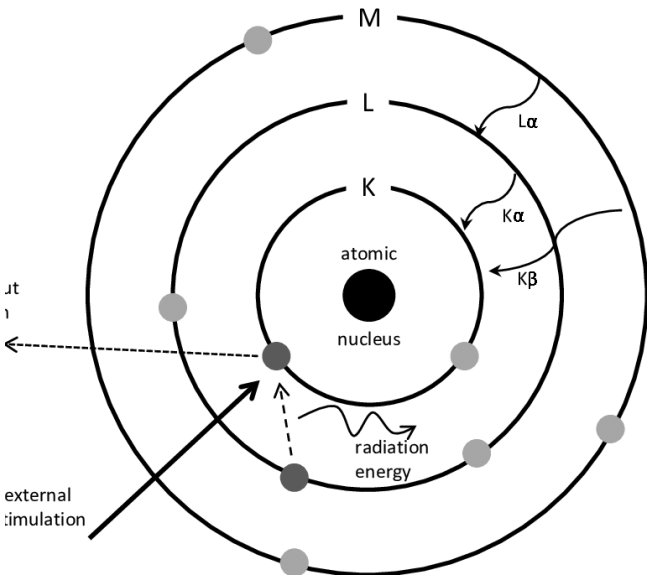

Figure 2.11: Schematic illustration of EDX operation: Incident electrons eject core-shell electrons, and the subsequent electronic transition results in the emission of element-specific X-ray photons.

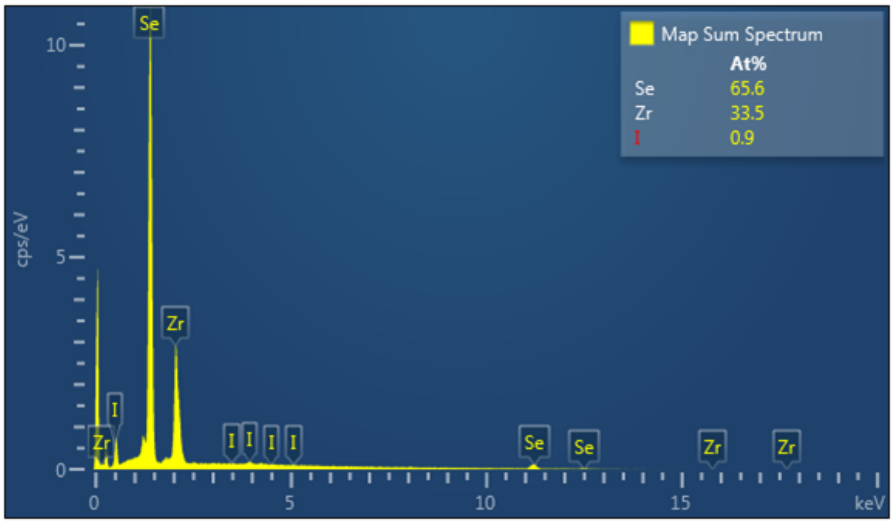

Figure 2.12: Typical EDX spectrum showing peaks for elemental analysis of a TMD sample.

influence electronic behavior [28].

The four-probe method is commonly employed for these measurements, as it effectively eliminates the influence of contact resistance and lead contributions [29]. In this method, a bar-shaped sample is mounted on a thermally stable platform using GE varnish or similar adhesive, and silver paste is used to establish ohmic contacts. These contacts are verified for both mechanical stability and electrical continuity prior to measurements.

The sample is placed in a cryogenic measurement system connected to a source-measure unit, nanovoltmeter, and temperature controller. The experiment is managed via a LabView interface, allowing for precise control of current, temperature sweep rate, and data acquisition. The chamber is first evacuated to achieve high vacuum, then cooled using a closed-cycle refrigerator.

A constant current is passed through the outer electrodes, and the voltage is measured across the inner electrodes while the temperature is varied gradually. At each thermal step, equilibrium is ensured before recording the voltage to avoid artifacts. The resistivity is calculated using the known dimensions of the sample and the measured voltage and current values [30].

This temperature-dependent resistivity data helps classify materials as metallic, semiconducting, or insulating, and can reveal phenomena such as metal-insulator transitions or charge ordering [31]. After completion, the system is carefully brought back to ambient conditions to prevent thermal shock.

Chapter 3

$ZrSe_2$

3.1 Introduction to $ZrSe_2$

Zirconium diselenide ($ZrSe_2$) is a layered material belonging to the class of transition metal dichalcogenides (TMDs). It consists of zirconium (Zr) atoms and selenium (Se) atoms in a stoichiometric ratio of 1:2. $ZrSe_2$ is part of the periodic table, where zirconium resides in the d-block of the 4th group, with an atomic number of 40. Selenium, a non-metal, belongs to the chalcogen group (group 16) and has an atomic number of 34. This combination of a transition metal and a chalcogen creates a compound with distinct properties that differ significantly from both the metal and the non-metal components [22, 23].

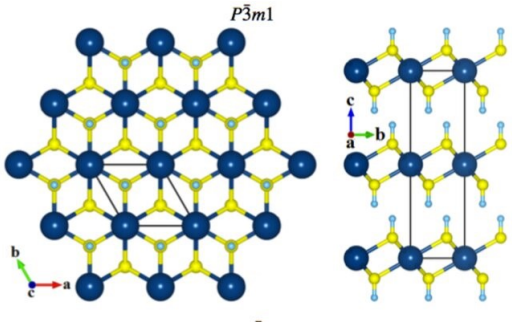

Figure 3.1: Crystal structure of $ZrSe_2$ representing the space group $P\bar{3}m1$ (No. 164).

$ZrSe_2$ crystallizes in a layered hexagonal structure, with zirconium (Zr) atoms sandwiched between two layers of selenium (Se) atoms. The layers are held together by weak van der Waals forces, which facilitate the exfoliation of the material into monolayers or thin films. Within each layer, the Zr and Se atoms are bound by strong covalent interactions, while the interaction between adjacent layers is much weaker, allowing for easy separation when mechanical forces are applied. The crystal

symmetry of $ZrSe_2$ is crucial in defining its electronic and optical properties, and these properties undergo significant changes when the material is reduced to a monolayer [22, 24].

The unique electronic, optical, and mechanical characteristics of $ZrSe_2$ make it a subject of great interest in materials science. Its layered structure positions it as a promising candidate for applications in 2D material-based devices, such as field-effect transistors and photodetectors, where the material's behavior is dramatically altered when reduced to a monolayer [23]. Additionally, $ZrSe_2$ is being investigated for its potential use in quantum computing and spintronic devices, as it may exhibit topologically non-trivial phases that could be harnessed in these advanced technologies [25,26]. Another promising area for research is the use of $ZrSe_2$ in thermoelectric applications, as its semiconducting properties could be exploited to convert heat into electricity efficiently [27]. Overall, $ZrSe_2$ serves as an important material for advancing current technologies and enabling new innovations in electronics, energy harvesting, and quantum computing.

3.1.1 Synthesis of $ZrSe_2$

$ZrSe_2$ is successfully synthesized using the CVT method. In the process, the stoichiometric ratios of Zr and Se are 1:2, and they are sealed in a quartz ampoule with iodine as the transport agent. The ampoule was placed inside a furnace. with temperatures maintained at 925°C (hot zone) and 810°C (cold zone) for 5 days with a temperature gradient of 115°C, and the reaction process took over five days to complete. During this process, $ZrSe_2$ crystals were transported and deposited in the colder end of the furnace.

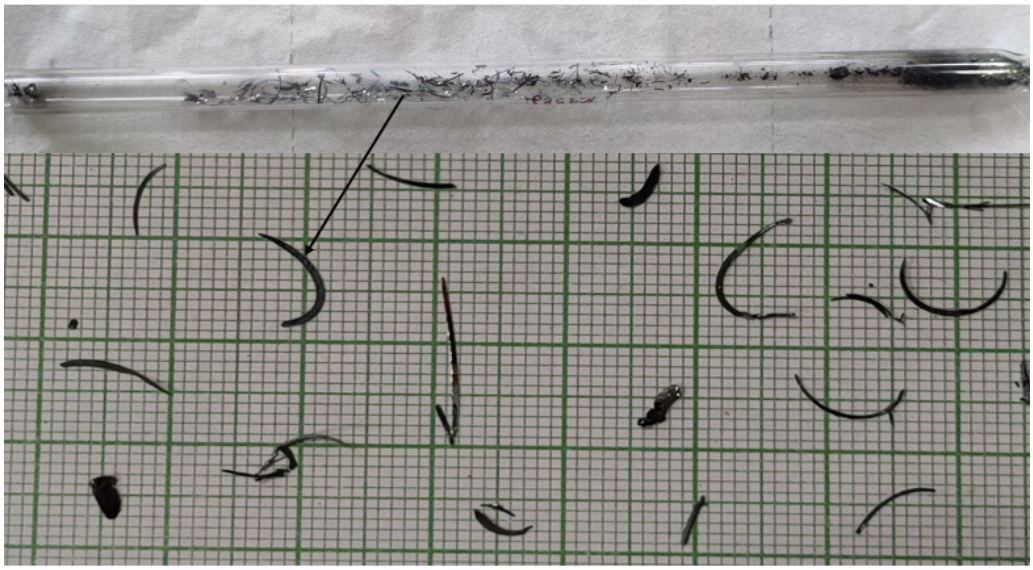

Figure 3.2: Fig. a) and b) Shows ZrSe2 Crystals Growths inside the ampoule by the CVT process.

3.1.2 X-ray Diffraction (XRD) analysis of $ZrSe_2$:

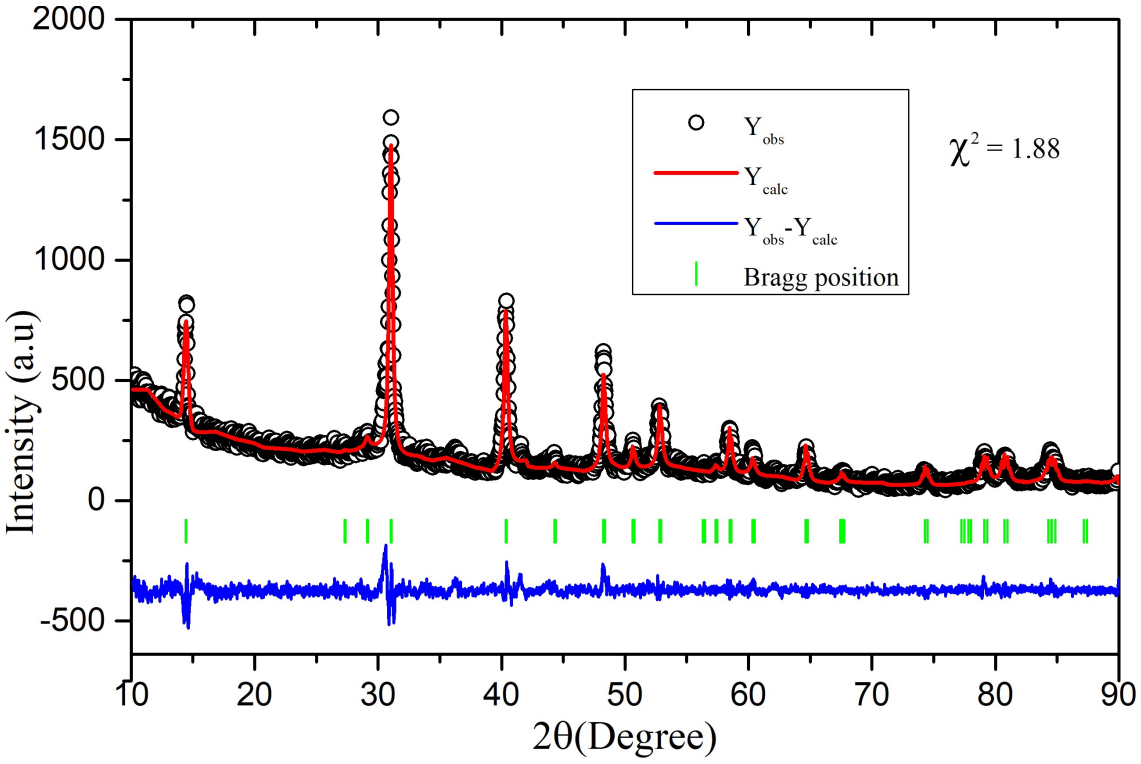

Figure 3.3: XRD pattern of $ZrSe_2$.

The X-ray diffraction (XRD) measurements for $ZrSe_2$ were carried out using a PANalytical Empyrean Alpha 1 diffractometer. This instrument was chosen due to its high sensitivity and ability to deliver reliable results with minimal sample amounts (0.0413 g in the experiment). The diffractometer uses monochromatic Cu-Kα radiation (wavelength λ = 1.5406Å) and operates in a high-resolution θ-θ geometry. The data was collected from a 2θ range of $10°$ to $90°$, with a step size of $0.03°$. To minimize noise and improve the quality of the diffraction data, the sample was carefully mounted on a low-background silicon substrate.

Table 3.1: Structural Parameters of the $ZrSe_2$

Parameter	**Value**
Space Group / Phase	P-3m1 (Trigonal)
Lattice Parameter $a = b$	3.76 Å
Lattice Parameter c	6.13 Å
Wyckoff Position (Zr and Se atoms)	2d (1/3, 2/3, z) O-25)2
Volume (V)	75.46(0.008) $Å^3$
Additional Parameter Chi2	1.87

The Rietvelt refinement is shown in Fig.3.3, demonstrating excellent agreement between the ob-

served and calculated Model.

The Rietveld refinement of $ZrSe_2$ resulted in a Chi^2 value of approximately 1.88, This indicates a strong agreement between the observed and calculated diffraction patterns. The refinement confirms that the sample crystallizes in the trigonal P-3m1 space group, and the unit cell coonstant $a = b = 3.7696$ Å and $c = 6.1326$ Å. The atomic positions of Zr and Se correspond to the Wyckoff position 2d $(1/3, 2/3, z)$, with $z \approx 0.25$. The unit cell volume was determined to be 75.4680 $Å^3$. The diffraction peaks align well with theoretical positions, confirming the layered structure characteristic of $ZrSe_2$, and no impurity peaks were detected, indicating high phase purity.

3.1.3 Raman Spectroscopy:$ZrSe_2$

To confirm its crystal structure and the synthesis process, Raman spectroscopy was used to characterize the synthesized $ZrSe_2$ sample. The crystal form of $ZrSe_2$ showed relevant Raman peaks, The observed patterns align with the vibrational modes of the material, as anticipated in the literature.

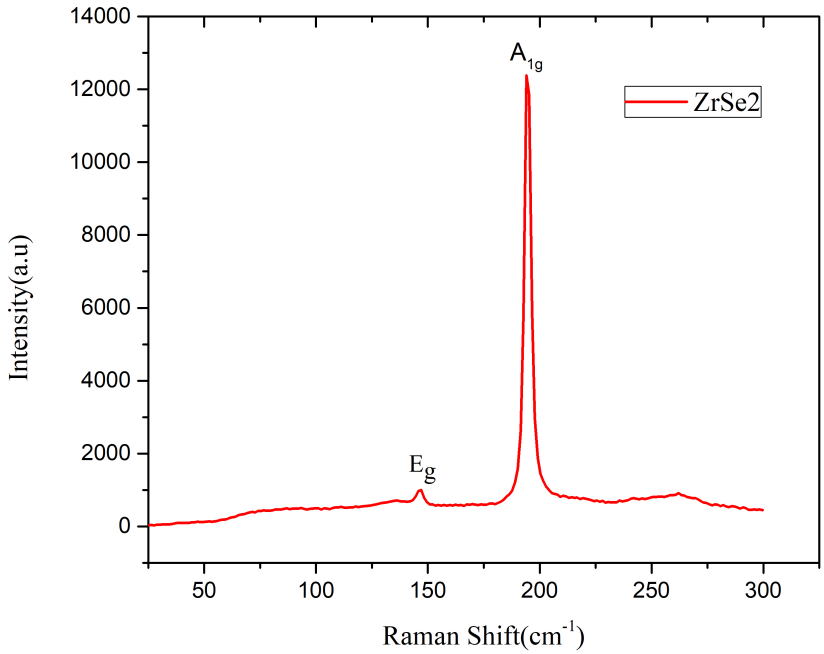

Figure 3.4: a) Raman spectrum of $ZrSe_2$ (λ = 633 nm). b) Shows the reference pattern of $ZrSe_2$ [12]

The Raman spectrum of $ZrSe_2$ shown in Fig. 6 a) shows a sharp, strongnear 195 cm^{-1}, which are the characteristic of the vibrational modes of $ZrSe_2$. This primary peak is due to the out of plane vibrational modes (A_{1g}) of the material. The well-defined nature of the peak suggest that the sample has good crystallinity. Additionally, smaller peaks observed in the lower wavenumber region (around

147 cm^{-1}) may correspond to in plane vibrations (E_g) or secondary phonon modes. The presence of main peaks in the spectrum indicates that the CVT grown $ZrSe_2$ Crystals have good structural quality.

Temperature-Dependent Raman Spectroscopy of $ZrSe_2$ Single Crystal

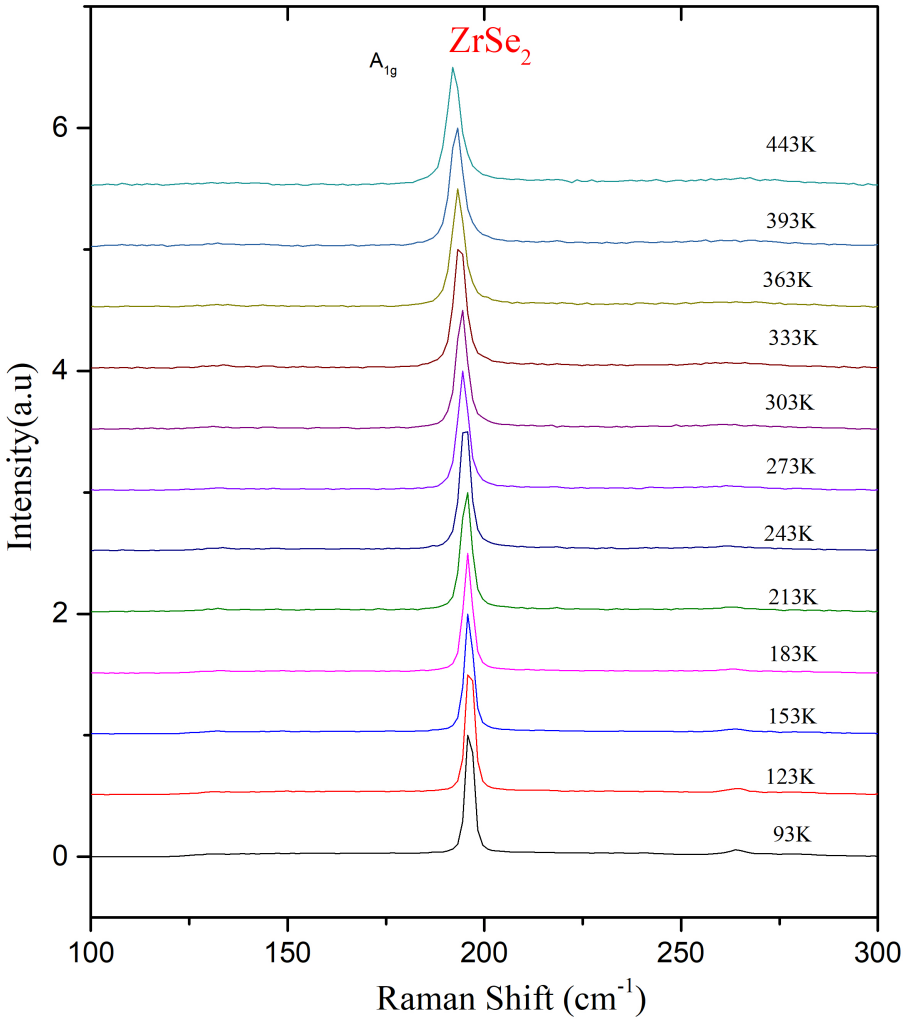

Figure 3.5: Temperature-dependent Raman spectra of $ZrSe_2$ single crystal measured from 93 K to 443 K. Only the A_{1g} mode near 195 cm^{-1} is visible throughout the range, while the expected E_g mode around 147 cm^{-1} is absent. With increasing temperature, a noticeable decrease in the intensity of the A_{1g} peak is observed, although its position remains unchanged. This suggests strong thermal stability of the vibrational mode without any structural phase transitions.

The Raman spectroscopic study of single crystalline $ZrSe_2$ was conducted over a wide temperature range, beginning at 93 K and gradually increasing up to 483 K. The primary objective of this investigation was to observe the behavior of the characteristic vibrational modes as a function of

temperature. In the Raman spectrum of $ZrSe_2$, the most prominent feature is the A_{1g} mode, which appears consistently near 195 cm^{-1} and corresponds to the out-of-plane vibrations of the selenium atoms. Notably, the in-plane E_g mode, which is generally expected around 147 cm^{-1} in such layered dichalcogenides, was not observed in the spectra at any temperature.

Throughout the entire temperature range, the position of the A_{1g} peak remained remarkably stable, exhibiting no significant shift with increasing temperature. This invariance in phonon frequency suggests that the vibrational dynamics of the crystal lattice are minimally affected by thermal expansion or anharmonic interactions within the probed range. Such behavior reflects the structural robustness of the $ZrSe_2$ lattice and the absence of any temperature-induced phase transitions during measurement [32].

Although the peak position remained unchanged, the intensity of the A_{1g} mode exhibited a gradual decline as the temperature increased. This reduction in Raman signal intensity at elevated temperatures is commonly attributed to enhanced phonon–phonon scattering and the increasing influence of thermal vibrations, which can reduce the efficiency of Raman scattering processes. These thermal effects result in damping of the vibrational modes, thereby lowering the intensity without necessarily affecting their energy.

The absence of the E_g mode across all temperatures may be due to orientation-dependent Raman selection rules, as well as the polarization configuration used during the measurement. In high-quality single crystals, certain vibrational modes may be suppressed or weakly visible depending on the crystallographic alignment with the excitation laser. Additionally, the mode may be inherently weaker or masked by background noise in the system.

In summary, temperature-dependent Raman analysis confirms the exceptional thermal stability of the A_{1g} mode in $ZrSe_2$ single crystals and suggests that the structural integrity of the material is preserved even at elevated temperatures. The monotonic decrease in peak intensity is a typical thermal effect and further supports the absence of structural transformation in this temperature regime.

3.1.4 SEM/ EDx Studies

To investigate the morphology and elemental composition of the synthesized $ZrSe_2$ crystals, scanning electron microscopy (SEM) and energy-dispersive X-ray spectroscopy (EDAX) were carried out. The SEM micrograph shown in Fig. 3.6B reveals a well-ordered layered surface, with long, parallel flakes characteristic of layered van der Waals materials. The morphology suggests successful crystal growth

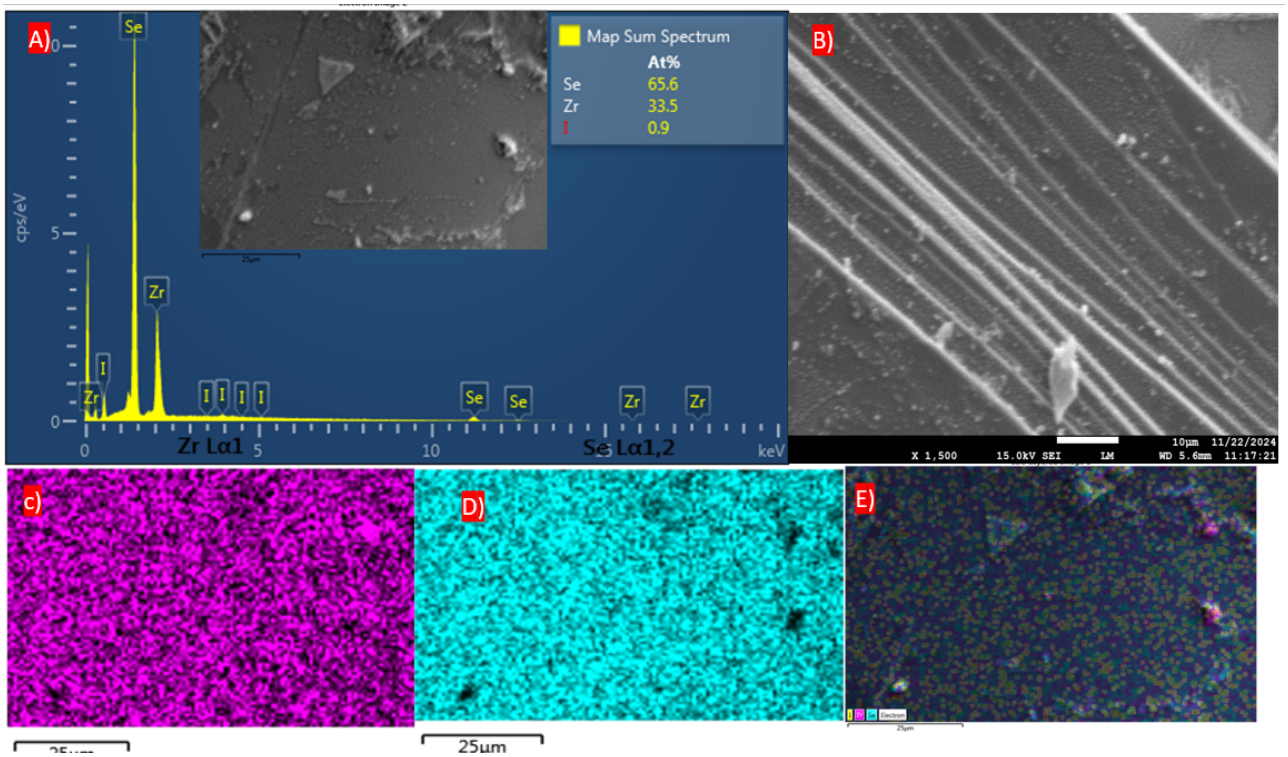

Figure 3.6: (A) EDX mapping spectrum of $ZrSe_2$ crystal, showing elemental composition with Se (65.6%), Zr (33.5%), and trace iodine (0.9%) along with an inset SEM image of the crystal surface. (B) SEM surface morphology of the synthesized $ZrSe_2$ crystal showing layered structure. (C) Elemental mapping of zirconium (Zr). (D) Elemental mapping of selenium (Se). (E) Combined elemental mapping showing the spatial distribution of Zr, Se, and trace iodine (I) across the sample.

Element	Experimental Atomic %	Ideal Atomic %	Atomic Ratio
Zr	**33.81%**	33.33%	1.00
Se	66.19%	66.67%	1.96

Atomic % and **Zr:Se ratio (~1:1.96)** compared with the ideal stoichiometry **(1:2)** of $ZrSe_2$.

via the chemical vapor transport (CVT) technique.

Elemental analysis was performed using EDAX, as illustrated in Fig. 3.6A. The corresponding spectrum confirms the dominant presence of zirconium and selenium, with atomic percentages of approximately 33.8% and 66.19%, respectively. The inset SEM image in Fig. 3.6A corresponds to the area scanned for compositional analysis.

Figures 3.6C and 3.6D present elemental mapping for zirconium and selenium, respectively. The uniform intensity across the scanned region indicates a homogeneous distribution of both elements throughout the crystal. Additionally, the composite mapping shown in Fig. 3.6E displays the spatial presence of Zr, Se, and iodine together, confirming the minimal and localized presence of iodine.

The slight selenium deficiency observed in the composition may lead to subtle shifts in electronic properties, such as the introduction of hole vacancies or increased carrier concentration due to zir-

conium excess. Such variations can influence the electronic structure of $ZrSe_2$, potentially driving it towards metallic or semimetallic behavior.

In summary, the SEM and EDAX analyses confirm that the synthesized $ZrSe_2$ crystal possesses a clean layered structure with near-stoichiometric composition and high elemental uniformity, validating the effectiveness of the CVT method used.

3.1.5 Resistivity measurment for $ZrSe_2$

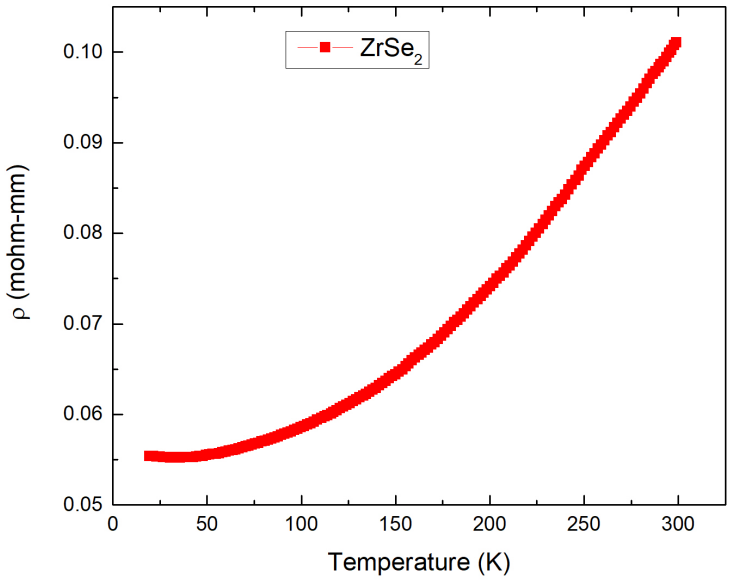

Figure 3.7: Temperature dependence of electrical resistivity (ρ) for $ZrSe_2$. The data show metallic behavior with resistivity gradually increasing from low to high temperatures.

The electrical resistivity (ρ) of the $ZrSe_2$ sample was examined over a temperature range spanning from 10 K to 300 K, as depicted in Figure 3.7. The measurements were performed using a standard four-probe configuration to eliminate contact resistance contributions. Throughout the measured range, the resistivity increases steadily with temperature, displaying a metallic trend.

At low temperatures near 10 K, the resistivity is found to be approximately 0.055 mΩ-mm. As the temperature rises, ρ gradually increases, reaching about 0.101 mΩ-mm at 300 K. Although an increase in resistivity with temperature is typically associated with semiconductors, the relatively low magnitude of resistivity values combined with the absence of activated behavior suggests metallic conduction.

The metallic character observed in $ZrSe_2$ can be linked to a slight zirconium enrichment detected

through Energy Dispersive X-ray Analysis (EDAX). A small excess of Zr atoms introduces additional charge carriers, effectively modifying the electronic structure and promoting metallic transport characteristics. Such sensitivity to stoichiometry is common among transition metal dichalcogenides, where deviations from the ideal composition can significantly alter their electronic properties.

Moreover, the smooth variation of ρ with temperature implies that the sample maintains good crystallinity and minimal defect scattering throughout the measurement range.

Chapter 4

$TiSe_2$

4.1 Introduction to $TiSe_2$

Titanium diselenide ($TiSe_2$) is a layered transition metal dichalcogenide (TMD) that has garnered significant interest due to its complex interaction between structural and electronic phenomena. Titanium, located in group 4 of the periodic table, combines with selenium from group 16 to form the stoichiometric compound $TiSe_2$. Structurally, $TiSe_2$ crystallizes in a 1T-type structure with the space group $P\bar{3}m1$, where each titanium atom is octahedrally coordinated by six selenium atoms. These layers are stacked along the c-axis and are bound by weak van der Waals forces, which contribute to $TiSe_2$'s characteristic quasi-two-dimensional nature.

At room temperature, $TiSe_2$ maintains an undistorted structure with Se–Ti–Se atomic layers arranged in a perfect sequence. In this phase, titanium atoms occupy the centers of octahedral prisms formed by the selenium atoms. The material behaves as a semimetal, with a small overlap between the valence band at the Γ point and the conduction band at the L point in the Brillouin zone.

When cooled below approximately 200 K, $TiSe_2$ undergoes a phase transition into a charge density wave (CDW) state, accompanied by a periodic lattice distortion (PLD). In this phase, the atoms experience slight displacements from their original positions, mainly within the basal plane, forming a $2a \times 2b \times 2c$ superlattice. The real-space unit cell expands along the a and b directions, a distinctive feature that can be observed by comparing the unit cells of the normal and CDW phases. This distortion is often represented as in-plane displacements of Ti and Se atoms, and the resulting CDW superstructure is characterized by a modulation of both the electronic charge density and atomic positions.

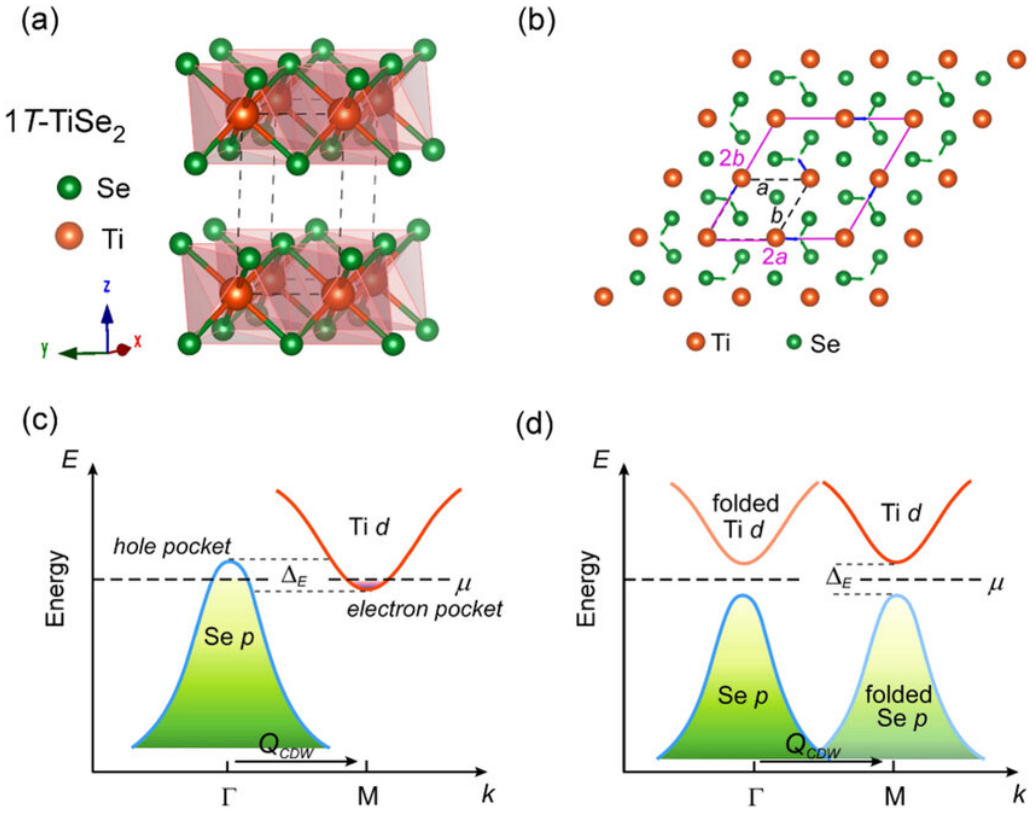

Figure 4.1: (a) Quasi-two-dimensional undistorted crystal structure of 1T-$TiSe_2$, showing the octahedral coordination of titanium and selenium atoms. (b) Top view illustrating the periodic lattice distortion (PLD) accompanying the charge density wave (CDW) transition, where arrows indicate the in-plane displacements of Ti and Se atoms. The dotted (black) lines represent the original unit cell in the normal phase, while the solid (pink) lines denote the enlarged unit cell in the CDW phase. (c) Schematic band structure near the Fermi level (E_F) in the normal phase, exhibiting an indirect band overlap. (d) Band structure in the CDW phase, showing back-folded bands and the opening of a bandgap due to the $2a \times 2b \times 2c$ PLD, making the Γ and M points equivalent. [34]

The PLD not only alters the real-space lattice but also significantly impacts the electronic band structure. In the CDW phase, the original bands fold back into the new, smaller Brillouin zone. This folding leads to the appearance of back-folded bands and the opening of a small energy gap near the Fermi level (E_F), transforming $TiSe_2$ from a semimetal into a material with semiconducting characteristics. Points that were distinct in the normal phase, such as the Γ and M points, become equivalent due to the new periodicity. The coupling between the electronic and lattice degrees of freedom in $TiSe_2$ makes it an ideal platform for studying fundamental condensed matter phenomena such as excitonic insulator behavior, CDW formation mechanisms, and the emergence of superconductivity under doping or pressure [34].

4.2 XRD Study of $TiSe_2$

To investigate the structural properties of the synthesized $TiSe_2$ material, powder X-ray diffraction (XRD) analysis was performed. Measurements were carried out using a Bruker D2 Phaser diffractometer equipped with a Cu Kα radiation source ($\lambda = 1.5406$ Å). The sample was mounted on a zero-background silicon holder to minimize background noise, and diffraction data were collected in a θ-2θ configuration over a 2θ range from $10°$ to $80°$, using a step size of $0.02°$.

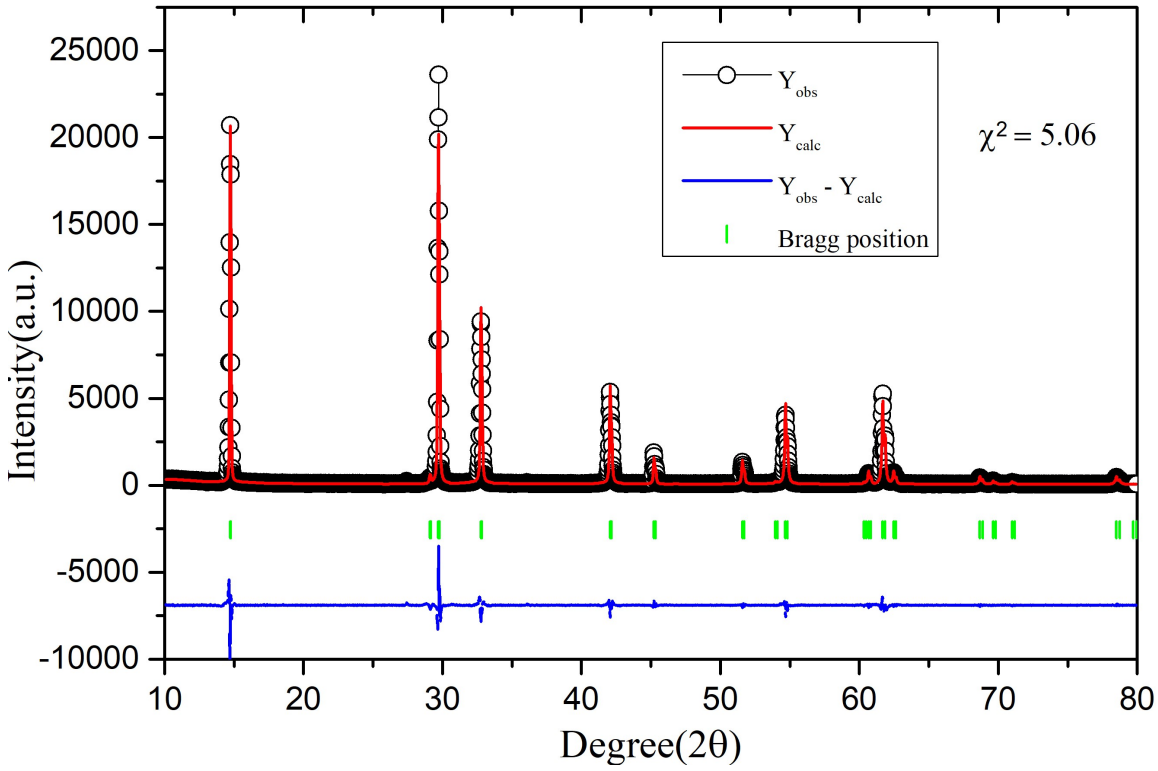

Figure 4.2: Powder XRD pattern of $TiSe_2$ synthesized in the laboratory.

Table 4.1: Structural parameters of $TiSe_2$ obtained from Rietveld refinement.

Parameter	**Value**
Space Group / Phase	P$\bar{3}$m1 (Trigonal)
Lattice Parameter $a = b$	3.50 Å
Lattice Parameter c	6.01 Å
Wyckoff Positions (atoms)	2d (1/3, 2/3, 0.23)
Unit Cell Volume (V)	65.23 Å^3
Chi^2 (Goodness of Fit)	5.06

The Rietveld refinement of the powder diffraction data confirms that the synthesized $TiSe_2$ crys-

tallizes in a trigonal phase with the P$\bar{3}$m1 space group, characteristic of the 1T polymorph. The extracted lattice constants were determined to be $a = 3.50\,\text{Å}$ and $c = 6.01\,\text{Å}$, closely matching the reported literature values. A goodness-of-fit value (Chi^2) of approximately 5.06 was achieved, indicating a reliable agreement between the experimental and calculated patterns. The sharp, well-defined diffraction peaks are indicative of high crystallinity, and the absence of secondary phase peaks confirms the high purity of the synthesized material.

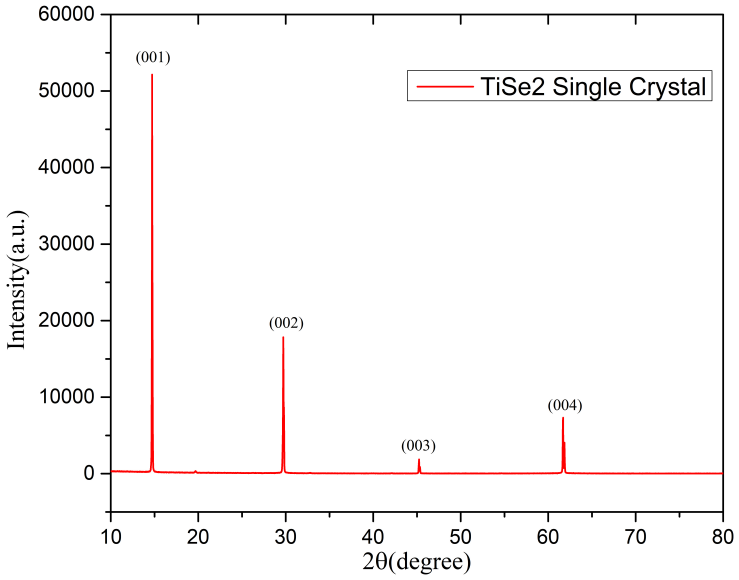

Figure 4.3: XRD pattern of single Crystal $TiSe_2$, displaying dominant (00l) reflections.

In addition to powder diffraction, XRD measurements were also conducted on a single crystal specimen of $TiSe_2$. The diffraction pattern, as shown in Figure 4.3, exhibits only a few sharp peaks corresponding to the (00l) reflections, such as (001), (002), and higher-order planes. The appearance of these specific reflections suggests that the crystal is highly oriented along the c-axis, consistent with the anisotropic, layered nature of $TiSe_2$. The sharpness and intensity of the peaks further emphasize the excellent crystallinity and preferred orientation of the single crystal.

The strong (00l) reflections are typical for van der Waals layered materials, where the crystallographic planes perpendicular to the c-axis dominate the diffraction profile. No extraneous reflections were observed, which supports the conclusion that the single crystal possesses high structural integrity and minimal mosaic spread. These observations collectively confirm the successful growth of high-quality $TiSe_2$ single crystals suitable for further physical property measurements, such as

Raman spectroscopy and transport studies.

4.3 Raman Study of $TiSe_2$

Raman spectroscopy is a powerful technique for probing the vibrational modes of materials, and in the case of $TiSe_2$, it offers valuable insights into its phonon modes and the temperature-dependent evolution of the charge density wave (CDW) phase. Bulk $TiSe_2$ exhibits two prominent Raman peaks that are crucial for understanding its structural and electronic properties: the in-plane E_g mode and the out-of-plane A_1g mode.

4.3.1 Raman Modes in $TiSe_2$

At room temperature, $TiSe_2$ exhibits two primary Raman active modes:

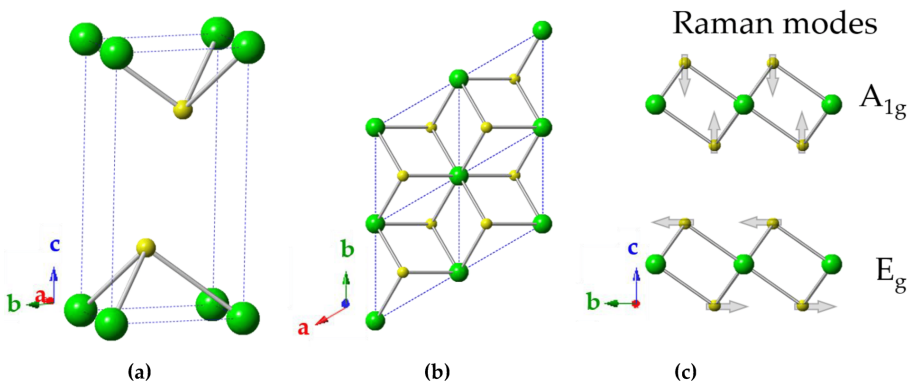

Figure 4.4: Showing the vibrational modes of Ti and Se atoms. [6]

- E_g at approximately 137 cm^{-1}: This is the in-plane doubly-degenerate mode, originating from the vibrations of Se atoms within the plane of the crystal.
- A_1g at approximately 195 cm^{-1}: This is the out-of-plane mode, corresponding to the vibrations of Ti atoms along the c-axis, perpendicular to the plane.

Both of these modes are characteristic of the undistorted crystal structure of $TiSe_2$, and their intensities and positions provide essential information about the material's symmetry and vibrational characteristics at various temperatures.

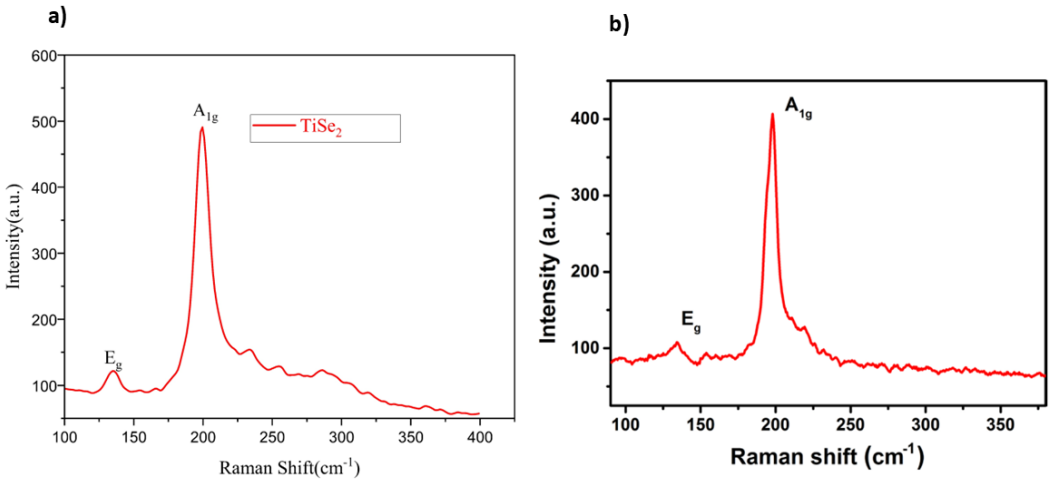

Figure 4.5: a) Raman spectrum of $TiSe_2$ at room temperature showing the prominent in-plane E_g and out-of-plane A_1g phonon modes.(λ = 633 nm). b) Shows the reference pattern of $TiSe_2$ [11]

4.3.2 Temperature-Dependent Raman Spectroscopy

Temperature-dependent Raman spectroscopy was performed on $TiSe_2$ over a wide range of temperatures, from 93 K to 443 K, to study the evolution of these phonon modes and the temperature-induced phase transition.

At temperatures below approximately 200 K, $TiSe_2$ undergoes a second-order phase transition into a commensurate charge density wave (CDW) state. This transition results in a distortion of the crystal lattice, which doubles the unit cell, forming a $2a \times 2a \times 2c$ superlattice. This distortion causes the Brillouin zone to fold and activates new Raman modes that are forbidden in the high-temperature phase.

In the CDW phase, additional Raman modes, known as **CDW amplitude modes**, emerge. These modes are associated with the transverse acoustic phonons at the zone boundary points (L and M). They are observed at lower wavenumbers (69 cm^{-1} for $E_g{}^{CDW}$ and 110 cm^{-1} for A_1g^{CDW}) and correspond to the in-phase and out-of-phase fluctuations of the CDW amplitude, respectively. The appearance of these modes indicates the formation and fluctuation of the CDW state.

As the temperature rises from 93 K to 443 K, significant changes are observed in the Raman spectra. The $E_g{}^{CDW}$ and A_1g^{CDW} modes experience a redshift and broadening of their peaks, with a corresponding decrease in their intensity. These spectral shifts reflect the weakening of the long-range order in the CDW phase due to thermal fluctuations. At temperatures above 200 K, these CDW modes gradually disappear, signaling the melting of the CDW state and the transition to a normal metallic phase.

Above the CDW transition temperature (T_{CDW} 205 K), only the original E_g and A_1g optical phonon modes remain. However, these modes also show slight redshifting and broadening as the temperature increases. This behavior is likely due to enhanced phonon-phonon interactions and possible electron-phonon coupling effects.

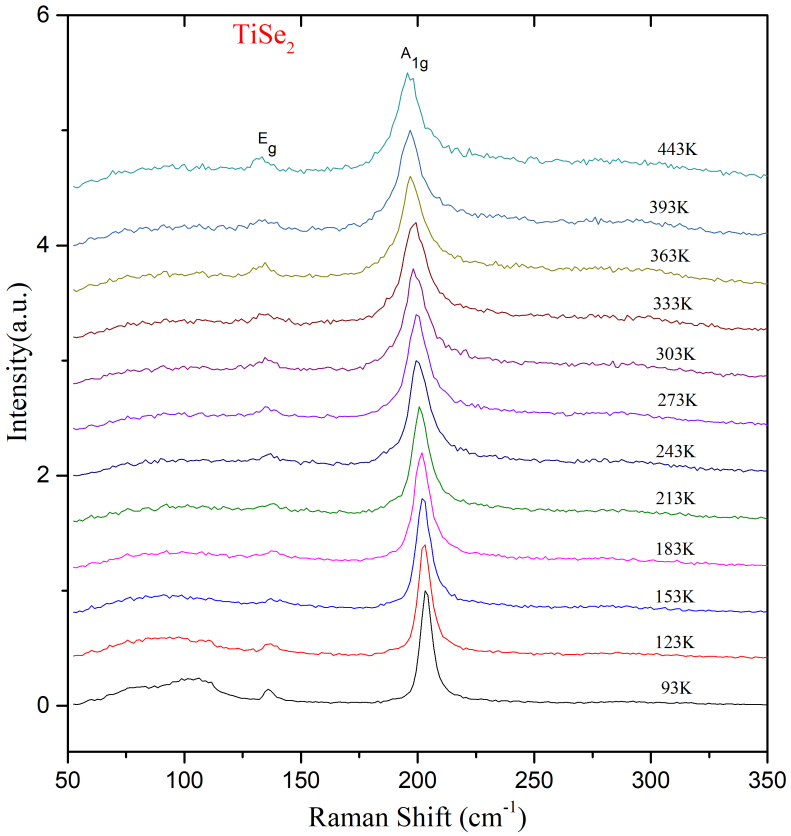

Figure 4.6: Temperature-dependent Raman spectrum of $TiSe_2$ showing the evolution of the E_g and A_1g modes, along with the emergence of CDW-related peaks below 200 K.

The temperature-dependent Raman behavior of $TiSe_2$ has been well-documented in the literature. According to Cu et al. [35], the CDW transition in bulk $TiSe_2$ occurs near 205 K. Below this temperature, additional Raman modes associated with the CDW phase emerge due to zone folding. These modes, $E_g{}^{CDW}$ at 69 cm^{-1} and A_1g^{CDW} at 110 cm^{-1}, become gradually softer (redshift) and broader with increasing temperature, corresponding to the weakening of the CDW order due to thermal fluctuations. These modes completely disappear above T_{CDW}.

Further, Snow et al. [36] describe the quantum melting of the CDW state in $TiSe_2$, emphasizing the softening and disappearance of the CDW modes as the temperature increases. They delineate

three distinct regimes of CDW behavior:

- **Crystalline CDW phase**: Sharp Raman peaks at low temperatures.
- **Fluctuating CDW phase**: Broadening and redshift of peaks at intermediate temperatures.
- **Melted CDW phase**: Disappearance of CDW modes at high temperatures, signifying the phase transition to a metallic, disordered state.

These phases are reflected in the evolution of the Raman spectrum of $TiSe_2$, which shows sharp peaks at low temperatures, gradual broadening and shifts at intermediate temperatures, and the eventual vanishing of the CDW peaks at higher temperatures.

The Raman study of $TiSe_2$ confirms the existence of a well-defined CDW phase below 205 K, with the corresponding activation of CDW-related Raman modes. As the temperature increases, these modes soften and vanish, indicating the melting of the CDW phase and the restoration of the normal metallic phase. The temperature-dependent evolution of the E_g and A_1g phonon modes provides critical insights into the phase transitions and the underlying electronic structure of $TiSe_2$. These findings align with previous studies and demonstrate the usefulness of Raman spectroscopy in probing the dynamics of the CDW phase in low-dimensional materials.

4.4 SEM and EDS Analysis

The morphology and elemental composition of the synthesized $TiSe_2$ sample were investigated using Scanning Electron Microscopy (SEM) coupled with Energy Dispersive X-ray Spectroscopy (EDS), as presented in Figure 4.7.

Figure 4.7a shows the EDS spectrum acquired from the sample surface. The prominent peaks corresponding to titanium (Ti) and selenium (Se) confirm the presence of the expected elements. Quantitative analysis reveals an atomic ratio of approximately 33.9% Ti and 66.1% Se, which is close to the ideal stoichiometry for $TiSe_2$. Minor peaks attributed to gold (Au) originate from the sputter-coating process used to improve surface conductivity during SEM imaging. The inset of Figure 4.7a displays a high-magnification SEM image highlighting the layered morphology typical of transition metal dichalcogenides.

Elemental mapping results are shown in Figure 4.7b, where Ti and Se distributions are presented separately along with an overlay image. Both elements appear uniformly distributed across

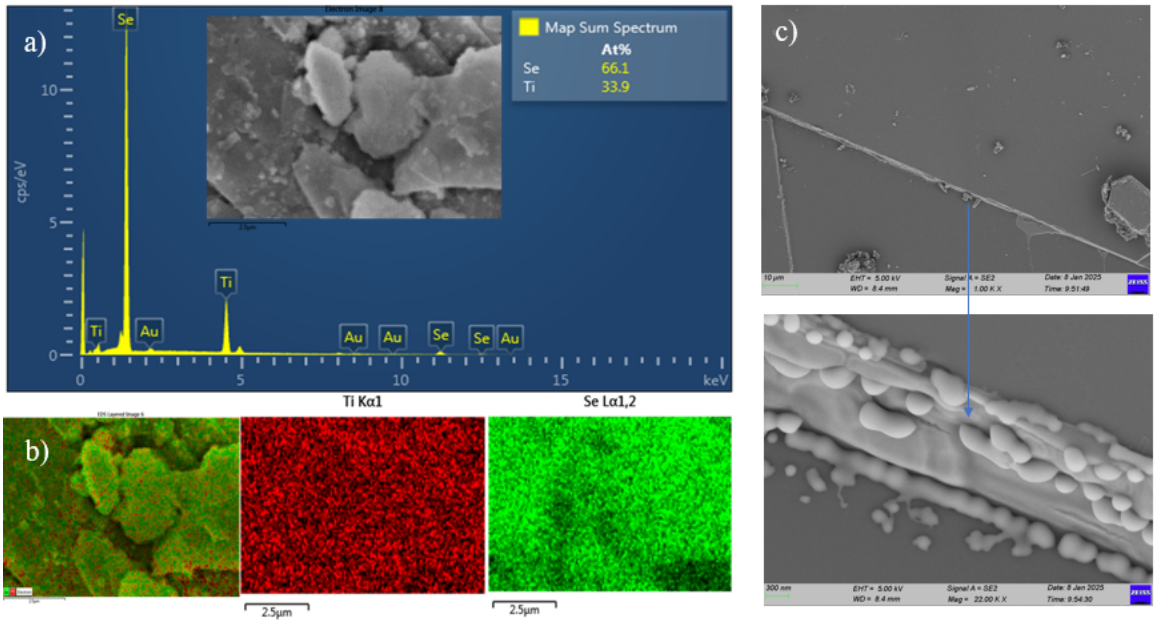

Figure 4.7: (a) EDS spectrum and corresponding SEM image of $TiSe_2$ sample, showing characteristic peaks of Ti and Se along with Au from coating. (b) Elemental mapping images displaying Ti (red), Se (green), and an overlay, indicating uniform distribution. (c) SEM micrographs at different magnifications revealing layered morphology and elongated structures.

the scanned region, suggesting good chemical homogeneity without significant phase segregation.

Additionally, low and high magnification SEM images (Figure 4.7c) reveal the formation of elongated structures alongside well-defined flakes. At higher magnifications, the layered growth nature and surface texture of the material are more evident. These observations align well with the expected growth habits of $TiSe_2$, confirming successful synthesis with high structural integrity.

Chapter 5

$ZrSe_3$

5.1 Introduction

Zirconium triselenide ($ZrSe_3$) is a member of the transition metal trichalcogenides (TMTCs) family, notable for its distinctive quasi-one-dimensional (quasi-1D) crystal structure and intriguing anisotropic properties [39]. Structurally, $ZrSe_3$ crystallizes in a monoclinic $P2_1/m$ space group, where zirconium atoms are coordinated by six selenium atoms to form distorted trigonal prisms. These prisms link together along the b-axis to produce chains, and adjacent chains are connected via weaker covalent bonds, forming layered structures stacked through van der Waals forces [37].

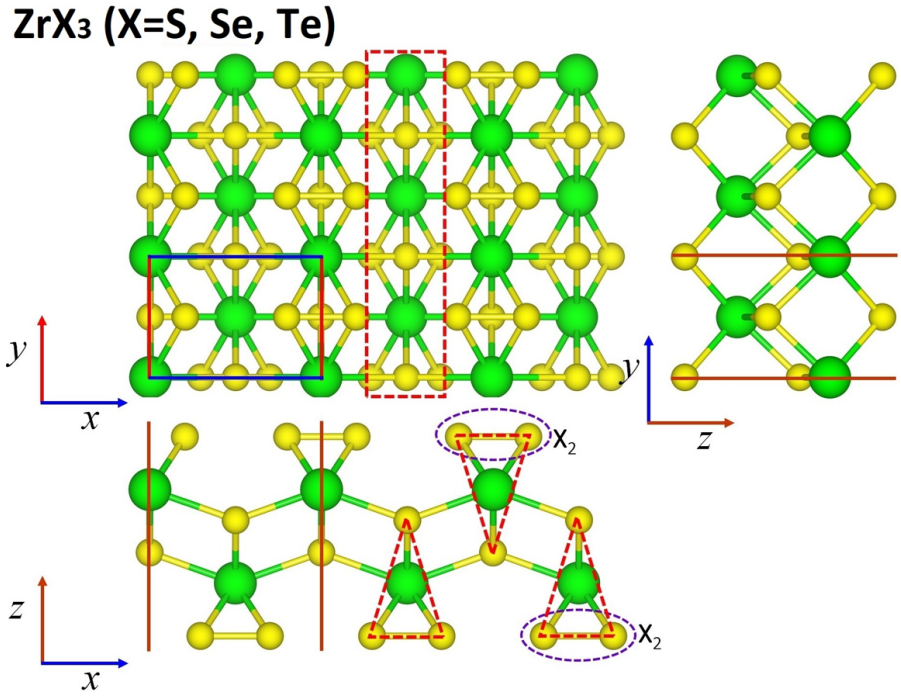

Figure 5.1: Crystal structure of $ZrSe_3$. Zirconium atoms (blue) form chains along the b-axis by connecting to selenium atoms (orange) in distorted trigonal prismatic coordination. Weak van der Waals forces hold the layers together along the c-axis.

This anisotropic architecture significantly influences the material's physical properties. Electrical and optical characterizations reveal that $ZrSe_3$ is a semiconductor, exhibiting an indirect band gap of approximately 1.1 eV and a direct gap around 1.47 eV [40]. Charge carrier transport is notably directional, with higher conductivity observed along the chain axis compared to the perpendicular directions. Furthermore, Raman spectroscopy studies have identified layer-dependent phonon modes, highlighting the quasi-1D nature of vibrational dynamics in $ZrSe_3$ [39].

From a thermal standpoint, $ZrSe_3$ displays moderate lattice thermal conductivity, peaking near 10.4 $Wm^{-1}K^{-1}$ at low temperatures, and decreasing with rising temperature [39]. The extracted Debye temperature of around 110 K reflects the relatively soft lattice dynamics, consistent with its low-dimensional structure. The calculated exfoliation energy for single-layer $ZrSe_3$ is approximately 0.37 Jm^{-2}, suggesting that mechanical exfoliation into few-layer nanosheets is feasible, similar to graphene [37].

Taken together, the unique chain-like bonding, directional anisotropy, and tunable semiconducting behavior make $ZrSe_3$ an appealing platform for future nanoelectronic, optoelectronic, and thermoelectric applications.

5.2 X-ray Diffraction Analysis

The crystal structure and phase purity of $ZrSe_3$ were analyzed using powder X-ray diffraction (XRD). High-quality single crystals were gently ground into fine powder to eliminate any preferential orientation effects. XRD measurements were performed using a PANalytical Empyrean Alpha-1 diffractometer equipped with a Cu Kα radiation source ($\lambda = 1.54$ Å).

Table 5.1: Refined structural parameters of $ZrSe_3$ from Rietveld analysis.

Parameter	**Value**
Space Group/Phase	$P2_1/m$, No. 11 / monoclinic
Lattice Parameter a	5.44 Å
Lattice Parameter b	3.77 Å
Lattice Parameter c	9.49 Å
Lattice Angles	$\alpha = 90.00°$, $\beta = 98.02°$, $\gamma = 90.00°$
Wyckoff Position (Zr and Se atoms)	2e sites with $y = 0.25$ and variable x and z
Direct Cell Volume (V)	193.04 $Å^3$
Goodness of Fit (χ^2)	6.78

The measured diffraction pattern and the results of Rietveld refinement are shown in Figure 5.2. Sharp, intense peaks were observed, indicative of the high crystallinity of the sample. The structural

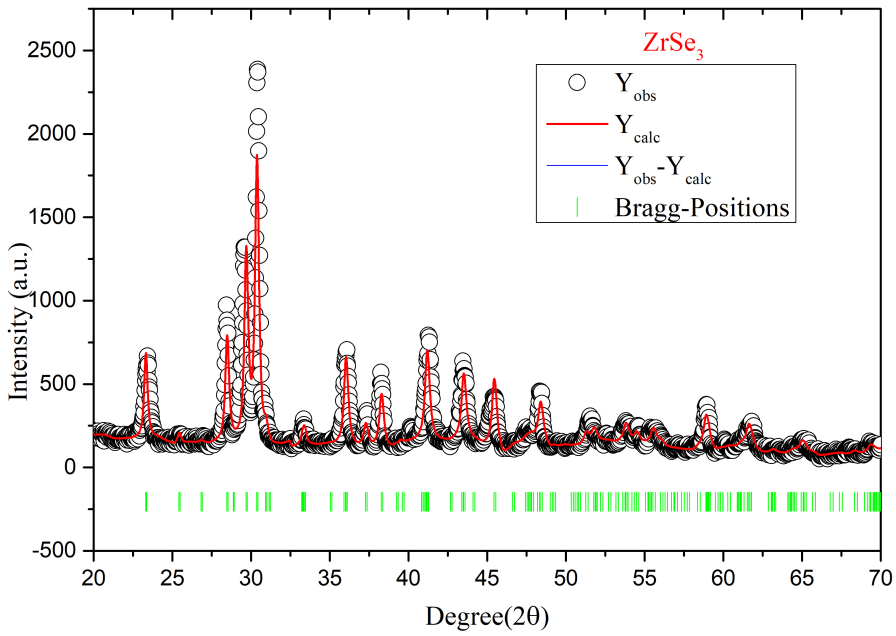

Figure 5.2: Rietveld refined X-ray diffraction pattern of $ZrSe_3$. Black circles represent observed data, the red curve is the calculated fit, and green ticks indicate Bragg reflection positions.

refinement was carried out using the crystallographic model reported by Furuseth *et al.* [38] for $ZrSe_3$, which adopts a monoclinic structure with the $P2_1/m$ space group. The refinement achieved a goodness-of-fit value of $\chi^2 = 6.78$, suggesting excellent agreement between the observed and calculated patterns.

The refined lattice parameters were found to be approximately $a = 5.41$ Å, $b = 3.75$ Å, $c = 9.47$ Å, and $\beta = 97.72°$, consistent with literature values [39,40]. No secondary phases were detected, confirming the high purity of the synthesized material.

Grinding the crystals into powder effectively randomized the crystallite orientations, minimizing the influence of texture. As a result, the intensities of the (00l) reflections typically strong in single crystals were suppressed, allowing an accurate structural determination.

In summary, the XRD results validate the successful synthesis of phase-pure, monoclinic $ZrSe_3$ with excellent crystallinity, making the sample suitable for further optical, electrical, and thermal property investigations.

5.3 Raman Spectroscopic Investigation of $ZrSe_3$

Raman spectroscopy was employed to study the vibrational properties of $ZrSe_3$ over a wide temperature range, from 93 K to 473 K. $ZrSe_3$ crystallizes in a monoclinic structure (space group $P2_1/m$), and group theoretical analysis predicts six Raman-active modes arising from Ag and Bg symmetries. The recorded Raman spectra at room temperature revealed five prominent peaks located approximately at 75 cm^{-1}, 110 cm^{-1}, 180 cm^{-1}, 240 cm^{-1}, and 310 cm^{-1}, as shown in Figure 5.3.

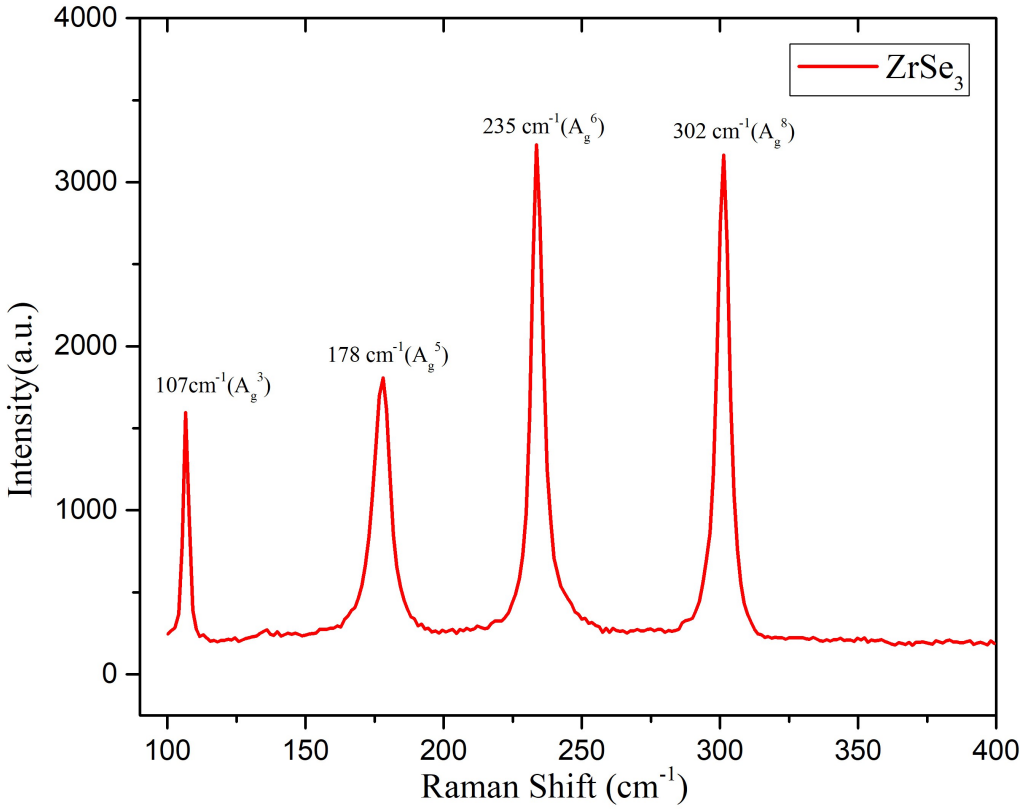

Figure 5.3: Room temperature Raman spectrum of $ZrSe_3$, with major vibrational modes marked.

These peaks correspond to different vibrational motions of Zr and Se atoms within the lattice, consistent with prior theoretical predictions [37] and experimental reports [40]. The modes observed around 75 cm^{-1} and 110 cm^{-1} can be attributed to low-frequency Bg-like and Ag-like vibrations, respectively, while the peaks near 180 cm^{-1} and 240 cm^{-1} arise from internal vibrations involving Zr–Se bond stretching and Se–Se dimers. The highest-frequency peak near 310 cm^{-1} is likely associated with higher-order lattice vibrations.

Upon lowering the temperature, an interesting behavior was observed: the peak located near 240 cm^{-1} at room temperature gradually split into two distinct components below approximately 200 K, as illustrated in Figure 5.4. This splitting is indicative of a subtle change in the vibrational

dynamics, possibly due to reduced thermal disorder and a lifting of phonon degeneracy at low temperatures.

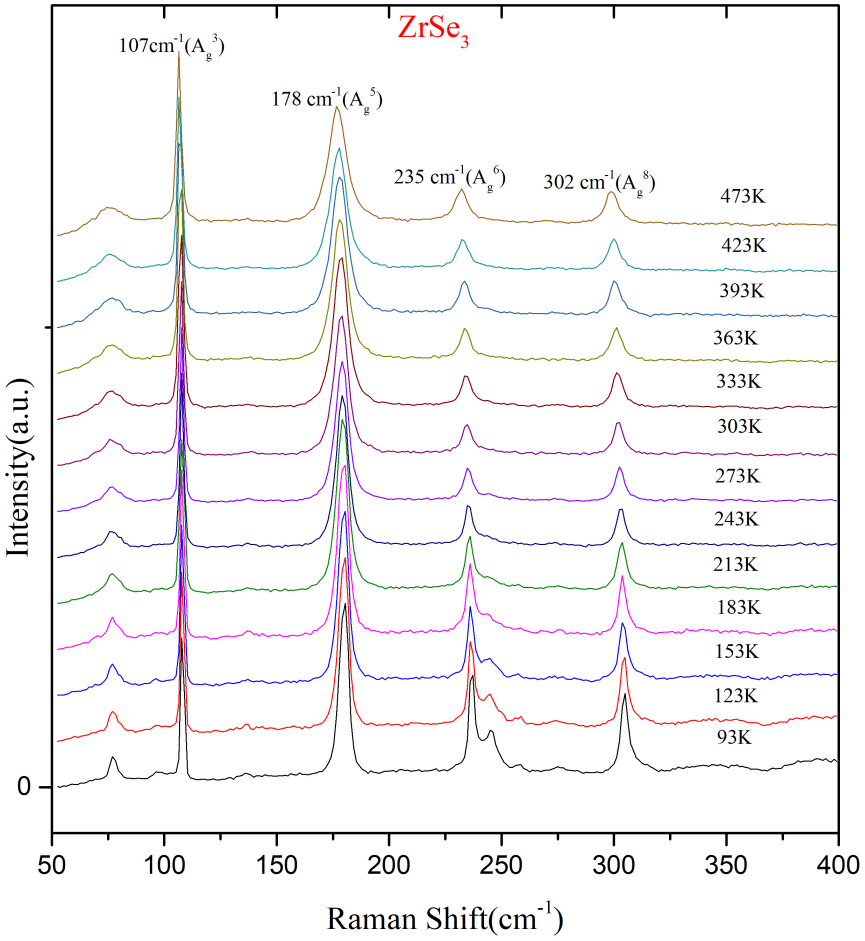

Figure 5.4: Low-temperature Raman spectra of $ZrSe_3$ showing the splitting of the $\sim$240 cm^{-1} mode.

Such phonon mode splitting has been reported in other layered materials and is typically attributed to weak interchain interactions and increased phonon lifetimes as temperature decreases. The overall sharpness and distinctness of the Raman peaks at lower temperatures also indicate a high degree of crystallinity and well-preserved structural order in the sample.

Comparison with previous theoretical and experimental studies confirms the validity of our observations. Mortazavi *et al.* [37] predicted strong Raman-active modes for $ZrSe_3$ at frequencies close to 220 cm^{-1}, 171 cm^{-1}, and 292 cm^{-1}, which are in good agreement with the peaks observed experimentally, considering slight shifts due to differences between monolayer and bulk forms. Additionally, the work by Patel *et al.* [40] discussed the semiconducting nature and optical properties of $ZrSe_3$,

supporting the stable lattice behavior inferred from Raman measurements.

In conclusion, the Raman spectroscopic investigation of $ZrSe_3$ reveals multiple vibrational modes corresponding to the monoclinic structure, and the low-temperature splitting of the 240 cm^{-1} peak provides evidence of subtle changes in the lattice dynamics. These results enhance the understanding of the vibrational behavior of $ZrSe_3$ and underline its potential for temperature-sensitive applications in electronic and optoelectronic devices.

5.4 SEM and EDS Analysis of $ZrSe_3$

The surface morphology and elemental composition of the synthesized $ZrSe_3$ crystals were examined using Scanning Electron Microscopy (SEM) coupled with Energy Dispersive X-ray Spectroscopy (EDS). The SEM images revealed that the $ZrSe_3$ crystals possess a layered and plate-like morphology, consistent with the expected lamellar structure of transition metal trichalcogenides. The layered arrangement, with relatively smooth and well-defined edges, reflects the good crystallinity and growth quality of the sample.

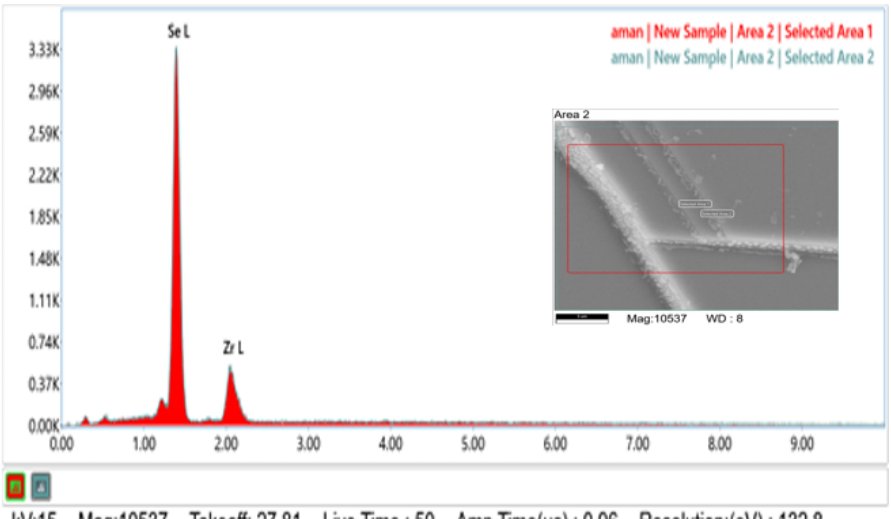

Element	Weight%	Atomic%
Zr	27.9	25.1
Se	72.1	74.9

Figure 5.5: EDS spectrum of $ZrSe_3$ confirming the presence of zirconium and selenium in near-stoichiometric ratio.No impurity elements are detected, supporting phase purity and successful synthesis.

To verify the elemental stoichiometry, EDS measurements were performed on several regions of the crystal surface. The corresponding EDS spectrum confirmed the presence of only zirconium (Zr)

and selenium (Se) elements, with no detectable impurities within the instrument's resolution limits. Quantitative analysis yielded a composition of approximately 27.9 wt% zirconium and 72.1 wt% selenium. In terms of atomic percentages, the Zr and Se contents were found to be 25.1% and 74.9%, respectively.

The atomic ratio obtained from EDS closely matches the ideal stoichiometric ratio expected for $ZrSe_3$, which theoretically consists of one zirconium atom to three selenium atoms. Minor deviations from exact values can be attributed to instrumental errors or slight surface non-uniformities during the measurement. Overall, the EDS analysis confirms the successful synthesis of stoichiometric $ZrSe_3$, supporting the results obtained from structural and vibrational studies.

Chapter 6

Isovalent Substitution in $ZrSe_2$ and $TiSe_2$: Synthesis and Study of $Zr_{0.05}Ti_{0.95}Se_2$ and $Ti_{0.05}Zr_{0.95}Se_2$

6.1 Introduction

After establishing the fundamental structural and electronic properties of pure $ZrSe_2$ and $TiSe_2$, the next step involves investigating the effects of isovalent substitution in these systems. Transition metal dichalcogenides (TMDCs) are highly sensitive to subtle changes in composition, which can significantly influence their physical properties. In this context, we have synthesized and studied two lightly substituted compounds: $Zr_{0.05}Ti_{0.95}Se_2$ and $Ti_{0.05}Zr_{0.95}Se_2$.

Although Ti^{4+} and Zr^{4+} ions are isovalent, their differences in atomic size and electronic structure can introduce notable modifications to the host lattice and band structure. Such substitutions can lead to phenomena like pseudodoping, where the material exhibits doping-like electronic behavior without actual carrier injection, as recently reported by Merentsov *et al.* [41].

The synthesis strategies were tailored to the characteristics of each system. For Ti-doped $ZrSe_2$ ($Ti_{0.05}Zr_{0.95}Se_2$), the compound was directly synthesized using the chemical vapor transport (CVT) method, with iodine as the transport agent. The starting powders were sealed in an evacuated quartz ampoule and subjected to a temperature gradient of 925°C at the hot end and 810°C at the cold end for a duration of five days.

In contrast, for Zr-doped $TiSe_2$ ($Zr_{0.05}Ti_{0.95}Se_2$), the synthesis involved a two-step process. Ini-

tially, a solid-state reaction was carried out, where Ti, Zr, and Se powders were thoroughly ground, pelletized, and heat-treated to obtain the polycrystalline phase. These pellets were then used as precursors for a second CVT growth step under similar thermal conditions to promote the formation of high-quality crystals.

The motivation behind exploring these materials lies in the opportunity to finely tune the electronic phases of $TiSe_2$ and $ZrSe_2$ through minimal isovalent substitution. $TiSe_2$ is known for its commensurate charge density wave (CDW) transition near 200 K, which is sensitive to external perturbations such as doping or pressure. $ZrSe_2$, on the other hand, is a semiconducting TMDC with an indirect bandgap. Introducing Zr into $TiSe_2$ offers a route to modify or suppress the CDW order via lattice distortions and electronic structure changes, while Ti substitution in $ZrSe_2$ may induce metallization or alter its semiconducting behavior. Understanding these effects is crucial for advancing our knowledge of pseudodoping phenomena and for developing strategies to engineer new electronic states in layered materials.

6.2 SEM and EDAX Analysis

To evaluate the morphology and elemental composition of the synthesized $Zr_{0.05}Ti_{0.95}Se_2$ and $Ti_{0.05}Zr_{0.95}Se_2$ samples, Scanning Electron Microscopy (SEM) and Energy-Dispersive X-ray Analysis (EDAX) were performed.

SEM imaging revealed clear differences in microstructure between the single crystalline and polycrystalline samples. The single crystals obtained through the chemical vapor transport (CVT) method displayed well-developed layered morphology with smooth surfaces and visible cleavage planes, characteristic of high-quality van der Waals crystals. In contrast, the polycrystalline samples exhibited a relatively rougher and more granular surface, indicating the typical grain growth associated with solid-state reaction methods.

Elemental analysis through EDAX further confirmed the successful incorporation of dopants into the host lattices. For the single crystal sample of Ti-doped $ZrSe_2$, the EDAX results showed:

Element	Weight %	Atomic %
Ti (K)	1.1	1.9
Se (L)	61.3	64.1
Zr (L)	37.6	34.0

Element	Weight %	Atomic %
Ti K	1.1	1.9
Se L	61.3	64.1
Zr L	37.6	34.0

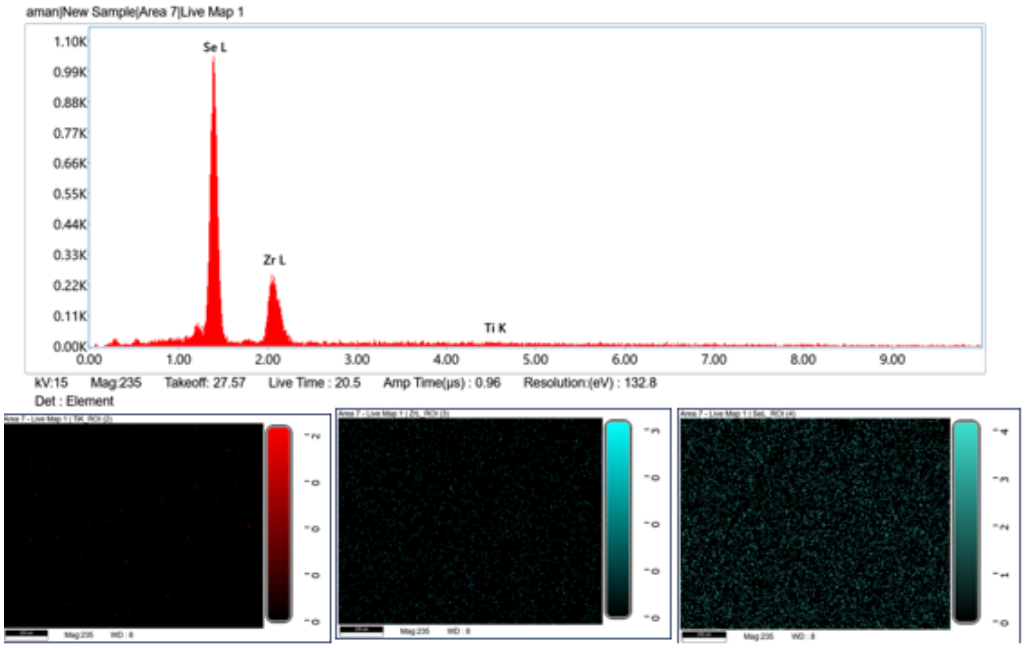

Figure 6.1: EDS spectrum confirming Zr, Se, and trace Ti presence in the expected ratio, supporting successful substitution.

The measured atomic percentages indicate a small amount of Ti substitution, close to the targeted 5% doping level. Slight deviations from the nominal composition are typical in EDAX measurements, especially at low doping concentrations, and can be attributed to factors such as sample surface roughness and instrumental sensitivity.

For the polycrystalline sample of Zr-doped $TiSe_2$, the EDAX data are summarized as follows:

Element	Weight %	Atomic %
Ti (K)	25.1	35.8
Se (L)	69.8	60.4
Zr (L)	5.1	3.8

In this case, the observed Zr content aligns well with the intended nominal composition of $Zr_{0.05}Ti_{0.95}Se_2$. The Se content remains relatively stable, suggesting minimal selenium loss during the synthesis and transport process.

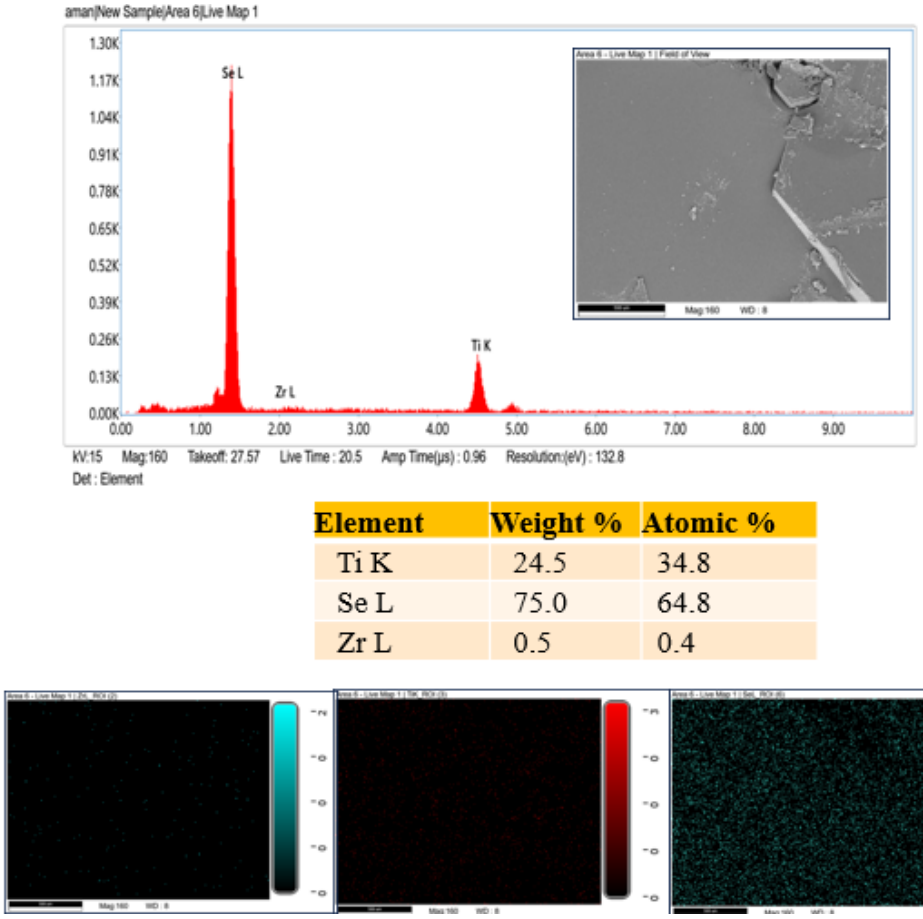

Element	Weight %	Atomic %
Ti K	24.5	34.8
Se L	75.0	64.8
Zr L	0.5	0.4

Figure 6.2: EDAX elemental mapping of Ti, Zr, and Se for single crystal Ti-doped $ZrSe_2$.

6.3 X-ray Diffraction Analysis

X-ray diffraction (XRD) studies were carried out to investigate the structural characteristics of $Zr_{0.05}Ti_{0.95}Se_2$ and $Ti_{0.05}Zr_{0.95}Se_2$ samples.

For Ti-doped $ZrSe_2$, due to the limited quantity of synthesized single crystals, it was not possible to perform powder X-ray diffraction (PXRD) by grinding the crystals. However, single crystal XRD measurements were conducted. The diffraction pattern revealed only four prominent peaks corresponding to the (00l) planes, characteristic of a layered structure with strong preferred orientation along the c-axis. This result is consistent with the expected structure of layered transition metal dichalcogenides and confirms the successful growth of single crystals, as shown in Figure 6.3.

In the case of Zr-doped $TiSe_2$, a sufficient amount of polycrystalline material was available, allowing PXRD measurements to be performed. The powder XRD pattern, shown in Figure 6.5, matched very well with the standard pattern of pristine $TiSe_2$, previously measured under identical conditions. This indicates that the substitution of a small amount of Zr into the $TiSe_2$ lattice does not significantly alter the overall crystal structure. Additionally, single crystal XRD was also performed on the

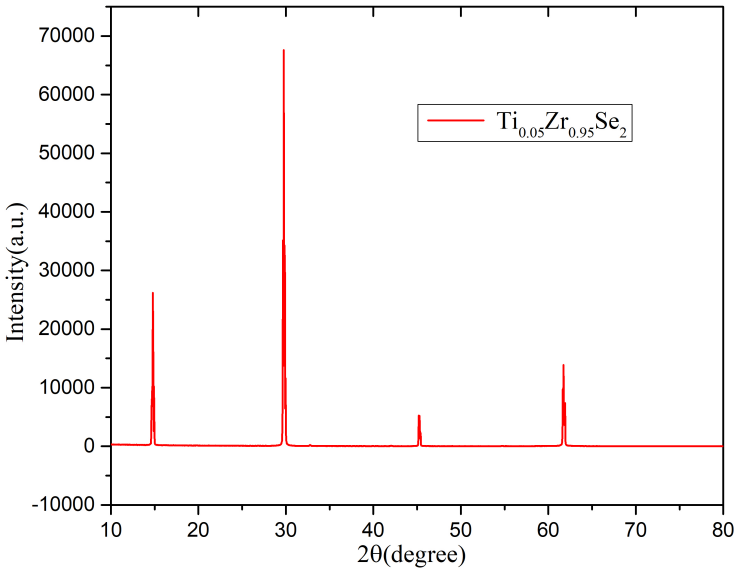

Figure 6.3: XRD pattern of Single crystal for Ti-doped $ZrSe_2$ showing sharp reflections.

Zr-doped $TiSe_2$ crystals (Figure 6.4), where, similar to pure $TiSe_2$, only four major peaks corresponding to the (00l) planes were observed, confirming the layered nature of the material.

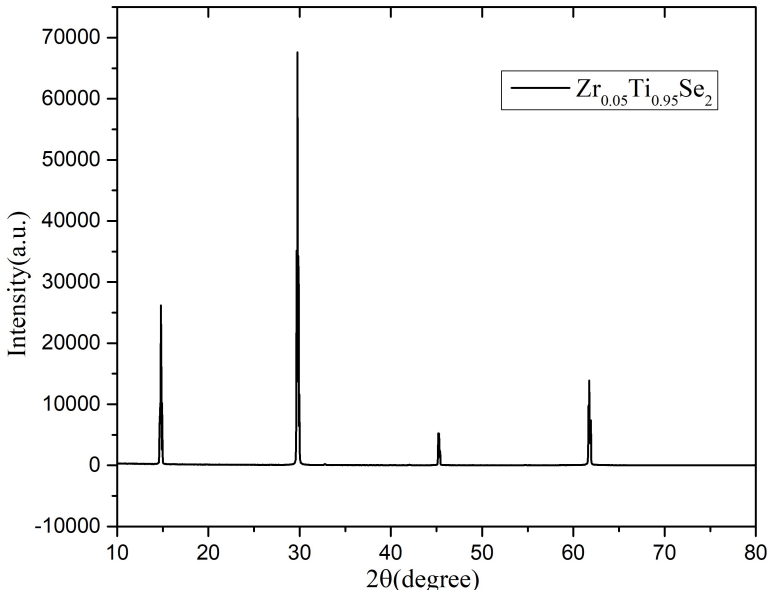

Figure 6.4: XRD pattern of Single crystal for Zr-doped $TiSe_2$ showing (00l) reflections.

Furthermore, Rietveld refinement was carried out on the PXRD data of the Zr-doped $TiSe_2$ polycrystalline sample. The refinement results Figure 6.5 showed excellent agreement with the experimental data, indicating a good fit and reaffirming the high phase purity and structural integrity of the synthesized material. The lattice parameters obtained from Rietveld refinement were found to be very close to those of undoped $TiSe_2$, suggesting that the incorporation of Zr at low concentration does not cause any significant distortion in the lattice.

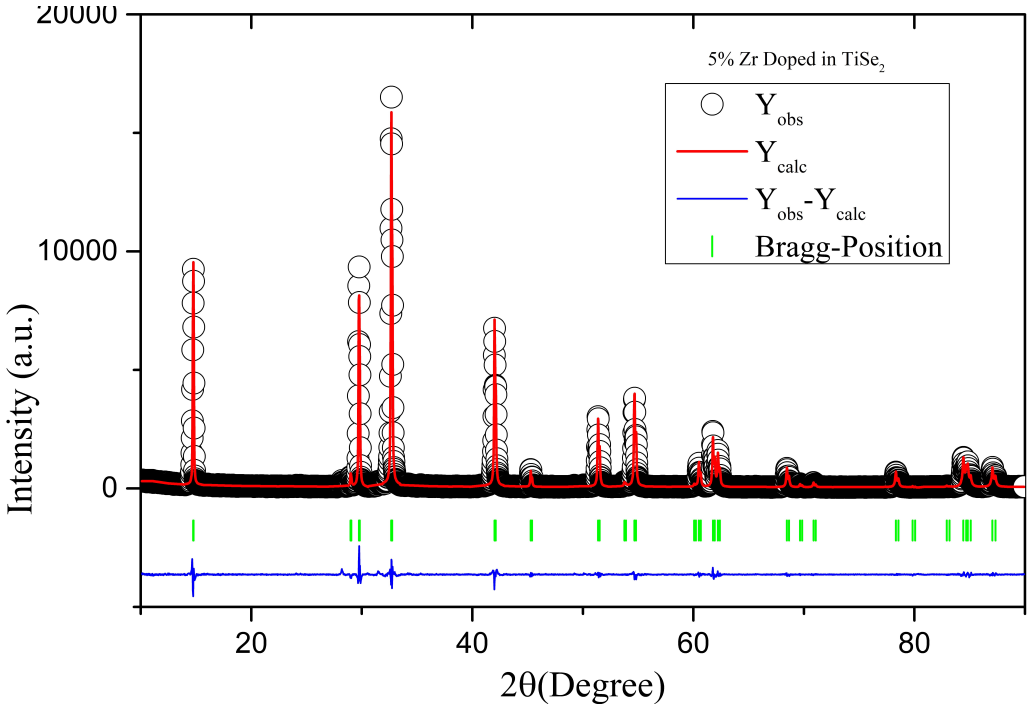

Figure 6.5: Rietveld refinement of PXRD pattern for Zr-doped $TiSe_2$.

Overall, XRD analysis confirms the successful doping and retention of the layered 1T structure

Parameter	Value
Space Group/Phase	P-3m1/Trigonal
Lattice Parameters	a = b= 3.55Å , c = 6.00Å
Wyckoff Positions (Ti&Se atoms)	1a(0,0,0) & 2d(1/3, 2/3, z);{z ~ 0.23}2
Volume (V)	65.65 Å³
$\chi 2$	2.81

in both Ti-doped $ZrSe_2$ and Zr-doped $TiSe_2$ systems.

6.4 Raman Spectroscopy

Raman spectroscopy was employed to investigate the vibrational properties and any subtle structural distortions arising from substitutional doping in $Zr_{0.05}Ti_{0.95}Se_2$ and $Ti_{0.05}Zr_{0.95}Se_2$. These measurements help to assess how the local environment and lattice dynamics respond to small compositional changes.

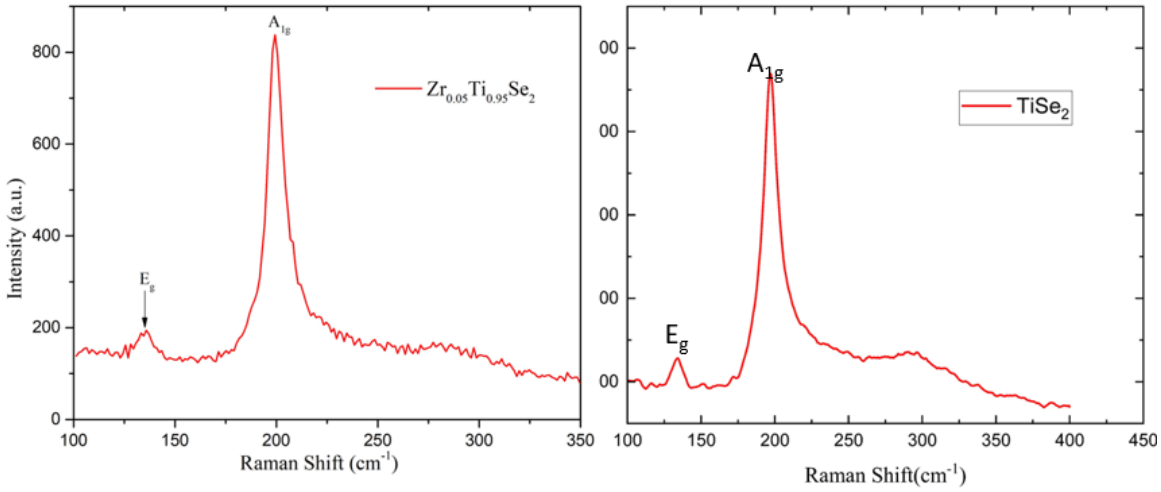

Figure 6.6: **Raman spectra of $Zr_{0.05}Ti_{0.95}Se_2$ and pristine $TiSe_2$.** Both spectra show characteristic E_g and A_{1g} vibrational modes of $ZrSe_2$, with no observable shift or broadening in the doped sample. This suggests that minor Ti substitution does not significantly alter the vibrational symmetry or structural integrity of the host lattice.

For **Zr-doped $TiSe_2$**, the Raman spectrum displays two dominant peaks at positions corresponding to the well-known E_g and A_{1g} modes of pristine $TiSe_2$. Importantly, the peak positions remain nearly unchanged even with the incorporation of approximately 0.4% Zr, as indicated by EDS analysis. This suggests that the symmetry and long-range vibrational behavior of the $TiSe_2$ lattice are largely preserved. The absence of any noticeable peak shift or splitting indicates that the low-level Zr

substitution does not introduce sufficient perturbation to distort the crystal field or break the degeneracy of vibrational modes. Thus, the Raman response confirms the structural stability and robustness of the host lattice against minor isovalent substitution.

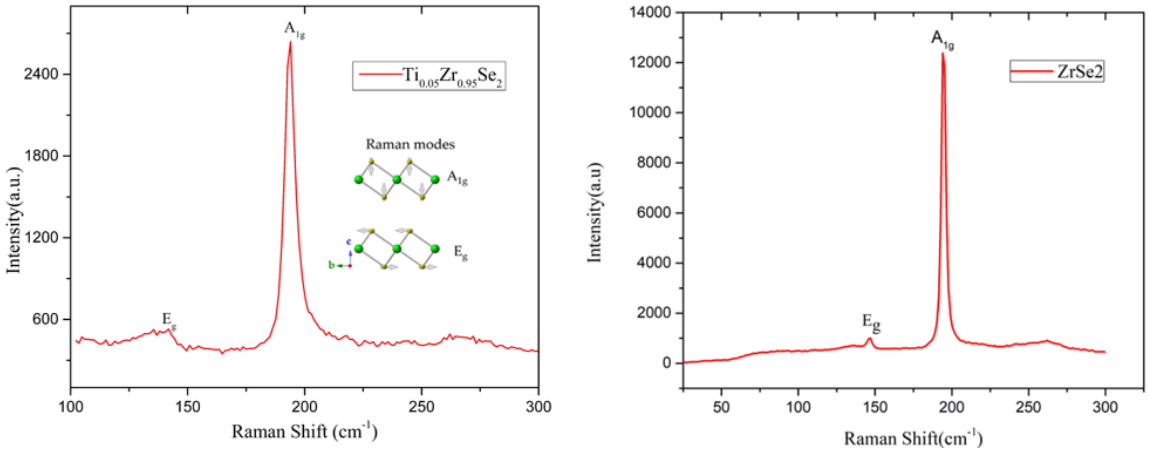

Figure 6.7: **Raman spectra of $Ti_{0.05}Zr_{0.95}Se_2$ and pristine $ZrSe_2$.** The characteristic E_g and A_{1g} modes are observed in both spectra. While peak positions remain largely unchanged, the Ti-doped sample exhibits a slight broadening of the E_g mode, attributed to local structural distortion from Ti substitution.

In contrast, the Raman spectrum of Ti-doped $ZrSe_2$ ($Ti_{0.05}Zr_{0.95}Se_2$) exhibits the characteristic E_{2g} and A_{1g} modes of $ZrSe_2$, located at frequencies similar to those in the undoped compound. However, a slight broadening of the E_{2g} peak is observed. This broadening is typically associated with local structural distortion or slight disorder in the lattice due to the presence of dopant atoms. Since Ti has a slightly smaller ionic radius than Zr and a marginally different bonding behavior, its presence at Zr sites may locally alter the vibrational coherence, leading to reduced phonon lifetime and hence peak broadening. Despite this, the retention of the main vibrational features and their positions suggests that the global symmetry of the crystal remains unaffected.

These observations reinforce the understanding that small isovalent substitution in layered transition metal dichalcogenides can introduce local modifications without substantially affecting the global lattice symmetry or phonon dynamics, especially when the substitution levels are minimal.

Chapter 7

Conclusion

This thesis presented a comprehensive structural and spectroscopic investigation of selected two-dimensional (2D) transition metal dichalcogenides (TMDs)—specifically $ZrSe_2$, $TiSe_2$, and $ZrSe_3$—alongside isovalently substituted derivatives such as $Zr_{0.05}Ti_{0.95}Se_2$ and $Ti_{0.05}Zr_{0.95}Se_2$. These materials were synthesized using the Chemical Vapor Transport (CVT) method, which yielded high-quality crystals with well-defined structural features.

X-ray diffraction (XRD) confirmed the phase purity and structural integrity of all samples. $ZrSe_2$ and $TiSe_2$ crystallized in the trigonal space group $P\bar{3}m1$, with sharp and intense (00l) reflections indicating excellent crystallinity and preferred orientation along the c-axis. In contrast, $ZrSe_3$, a member of the trichalcogenide family, exhibited a monoclinic structure with chain-like motifs, resulting in a more complex diffraction pattern due to its quasi-one-dimensional geometry and reduced symmetry.

Raman spectroscopy was used to probe vibrational characteristics and confirm crystal structures. $ZrSe_2$ displayed a dominant A_{1g} mode near 195 cm^{-1}, which remained stable across a broad temperature range (93 K to 483 K), showing only a gradual decrease in intensity—indicative of thermal stability and the absence of any structural phase transitions. $TiSe_2$ exhibited a temperature-dependent Raman response consistent with a charge density wave (CDW) transition below approximately 200 K. New low-frequency modes appeared in this regime, attributed to CDW amplitude fluctuations, and vanished at higher temperatures, confirming the reversibility of the phase transition.

A notable result emerged from the temperature-dependent Raman study of $ZrSe_3$. Due to its lower monoclinic symmetry, $ZrSe_3$ displayed more complex phonon behavior compared to the higher-symmetry compounds. As temperature decreased, one prominent Raman mode exhibited a clear splitting into two components. This splitting is attributed to the lifting of degeneracy and enhanced

phonon anisotropy resulting from symmetry-lowering and directional bonding, further emphasizing the quasi-one-dimensional character of $ZrSe_3$.

Field Emission Scanning Electron Microscopy (FESEM) and Energy Dispersive X-ray Spectroscopy (EDX) confirmed clean, layered morphologies and near-stoichiometric compositions for all samples. Minor deviations, such as Zr enrichment in $ZrSe_2$, were found to influence electrical resistivity, possibly via unintentional doping. Trace iodine from the CVT process was detected but did not significantly affect the structural or vibrational properties.

Electrical resistivity measurements supported these observations. $ZrSe_2$ displayed metallic-like behavior with increasing resistivity as temperature rose, likely linked to off-stoichiometry. $TiSe_2$ demonstrated semimetallic characteristics with features associated with the CDW transition.

In conclusion, the interplay of crystal structure, symmetry, and stoichiometry has been shown to critically influence the vibrational and electronic behavior of 2D TMDs. Observations such as phonon mode splitting in $ZrSe_3$ and temperature-dependent CDW signatures in $TiSe_2$ highlight the sensitivity of these materials to structural changes, paving the way for their use in tunable optoelectronic and low-dimensional quantum devices.

Bibliography

[1] M. Chhowalla, H. S. Shin, G. Eda, L.-J. Li, K. P. Loh, and H. Zhang, *The Chemistry of Two-Dimensional Layered Transition Metal Dichalcogenide Nanosheets*, Nature Chemistry, vol. 5, no. 4, pp. 263–275, 2013. DOI: 10.1038/nchem.1589

[2] A. Splendiani, L. Sun, Y. Zhang, T. Li, J. Kim, C.-Y. Chim, G. Galli, and F. Wang, *Emerging Photoluminescence in Monolayer MoS_2*, Nano Letters, vol. 10, no. 4, pp. 1271–1275, 2010. DOI: 10.1021/nl903868w

[3] J. A. Wilson and A. D. Yoffe, *The Transition Metal Dichalcogenides Discussion and Interpretation of the Observed Optical, Electrical and Structural Properties*, Advances in Physics, vol. 18, no. 73, pp. 193–335, 1969. DOI: 10.1080/00018736900101307

[4] W. J. Schutte, J. L. De Boer, and F. Jellinek, *Crystal Structures of Titanium Disulfide and Zirconium Disulfide*, Journal of Solid State Chemistry, vol. 70, no. 2, pp. 207–209, 1987. DOI: 10.1016/0022-4596(87)90008-4

[5] B. D. Cullity and S. R. Stock, *Elements of X-ray Diffraction*, 3rd ed., Prentice Hall, 2001.

[6] S. Mañas-Valero, E. Coronado, A. Ribera, and E. Navarro-Moratalla, *Raman Spectra of ZrS_2 and $ZrSe_2$ from Bulk to Atomically Thin Layers*, Applied Sciences, vol. 6, no. 9, p. 264, 2016. DOI: 10.3390/app6090264

[7] Long, D. A., "The Raman Effect: A Unified Treatment of the Theory of Raman Scattering by Molecules," John Wiley & Sons, 2002.

[8] Barron, A. R., and Raja, P. M. V., "4.03: Raman Spectroscopy," *LibreTexts Chemistry*, `https://chem.libretexts.org/Bookshelves/Physical_and_Theoretical_Chemistry_Textbook_Maps/Supplemental_Modules_`

(Physical_and_Theoretical_Chemistry)/Spectroscopy/Vibrational_Spectroscopy/Raman_Spectroscopy.

[9] Wikipedia contributors, "Raman spectroscopy," *Wikipedia, The Free Encyclopedia*, https://en.wikipedia.org/wiki/Raman_spectroscopy.

[10] TLP Library, "Raman Spectroscopy – Active Modes," *Department of Materials Science and Metallurgy, University of Cambridge*, https://www.doitpoms.ac.uk/tlplib/raman/active_modes.php.

[11] X. Zhang, Y. Han, J. Wu, S. Milana, Y. Lu, Q. Li, A. C. Ferrari, and P. H. Tan, *Raman Spectroscopy of Shear and Layer Breathing Modes in Multilayer MoS_2*, Physical Review B, vol. 87, no. 11, p. 115413, 2013. DOI: 10.1103/PhysRevB.87.115413

[12] Z. Hong, et al., *Optics and Photonics Journal*, vol. 10, no. 8, pp. 251–263, 2020. DOI: 10.4236/opj.2020.108020

[13] B. Ghosh, et al., *Phys. Rev. B*, vol. 106, no. 10, p. 104102, 2022. DOI: 10.1103/PhysRevB.106.104102

[14] R. Bhatt, et al., *AIP Conf. Proc.*, vol. 1536, p. 881, 2013. DOI: 10.1063/1.4810510

[15] Mortazavi, et al. , *A Theoretical Investigation on the Physical Properties of Zirconium Trichalcogenides, ZrS_3, $ZrSe_3$ and $ZrTe_3$ Monolayers*. Energies, vol. 15, no. 15, 2022, p. 5479. DOI: 10.3390/en15155479

[16] W. Salomons and G. A. Wiegers, *The System Zirconium-Selenium: Structures of the Phases Zr_3Se_6 and Zr_5Se_3*, Laboratorium voor Anorganische Chemie, Rijksuniversiteit, 2010.

[17] M. Berger, Q. Yang, and A. Maier, "X-ray Imaging," in Medical Imaging Systems: An Introductory Guide, A. Maier, S. Steidl, V. Christlein, et al., Eds. Cham, Switzerland: Springer, 2018. https://www.ncbi.nlm.nih.gov/books/NBK546155/figure/ch7.fig8/

[18] A. A. Bunaciu, E. G. Udriştioiu, and H. Y. Aboul-Enein, "X-Ray Diffraction: Instrumentation and Applications," Critical Reviews in Analytical Chemistry, vol. 45, no. 4, pp. 289–299, 2015, doi: 10.1080/10408347.2014.949616.

[19] C. V. Stan, C. M. Beavers, M. Kunz, and N. Tamura, "X-Ray Diffraction under Extreme Conditions at the Advanced Light Source," Instruments, vol. 2, no. 1, pp. 1–13, Jan. 2018, doi: 10.3390/instruments2010002.

[20] L. Robles-Gómez, P. Sáez-Espinosa, and M. J. Gómez-Torres, "Field Emission Scanning Electron Microscopy (FE-SEM) as an Approach for Membrane Surface Mapping in Cell Biology," in Spermatology, Methods in Molecular Biology (MIMB), vol. 2897, pp. 435–444, Springer, 2025, doi: 10.1007/978-1-0716-4703-633.

[21] "Field Emission Scanning Electron Microscope (ZEISS Gemini)," Indian Institute of Technology Roorkee (IITR),https://www.iitr.ac.in/Centres/Institute

[22] J. Zhao, Y. Zhang, L. Wang, X. Wu, Z. Lu, and Z. Zhang, "High-quality $ZrSe_2$ single crystals and their characterization," *J. Mater. Chem. C*, vol. 5, no. 12, pp. 3060-3068, 2017.

[23] Y. Wang, L. Zhang, Y. Li, Y. Liu, X. He, and Z. Zhou, "Layered $ZrSe_2$: Synthesis, properties, and potential applications in 2D electronics," *Adv. Mater.*, vol. 31, no. 20, p. 1806489, 2019.

[24] Y. Liu, Z. Wei, Y. Li, X. Liu, and S. Zhang, "Ultrafast charge transport in $ZrSe_2$ monolayers," *Nano Lett.*, vol. 20, no. 9, pp. 6782-6787, 2020.

[25] Z. Li, Y. Li, X. Zeng, Y. Xie, and F. Wang, "Topological phases in $ZrSe_2$ and their quantum computing applications," *Nat. Mater.*, vol. 20, no. 11, pp. 1342-1347, 2021.

[26] S. Zhang, J. Liu, Y. Wang, and L. Xu, "Spintronics and topological properties of $ZrSe_2$," *Nat. Commun.*, vol. 11, no. 1, pp. 1-9, 2020.

[27] H. Yang, W. Wu, X. Zhou, and L. Zhang, "Thermoelectric performance of $ZrSe_2$: An experimental and computational study," *Adv. Energy Mater.*, vol. 9, no. 16, p. 1900797, 2019.

[28] Sze, S. M., and Ng, K. K., "*Physics of Semiconductor Devices*," 3rd ed., Wiley-Interscience, Hoboken, NJ, 2006.

[29] Montgomery, H. C., "Method for Measuring Electrical Resistivity of Anisotropic Materials," *Journal of Applied Physics*, vol. 42, no. 7, pp. 2971–2975, 1969.

[30] Kittel, C., "*Introduction to Solid State Physics*," 8th ed., Wiley, New York, 2005.

[31] Mott, N. F., “Metal-Insulator Transition,” *Reviews of Modern Physics*, vol. 40, no. 4, pp. 677–683, 1968.

[32] M. Sugai and T. Ueda, ”High-pressure Raman spectroscopy in the layered materials 1T-ZrS_2, 1T-$ZrSe_2$ and 2H-MoS_2,” *Phys. Rev. B*, vol. 26, no. 12, pp. 6554–6558, 1982.

[33] F. J. Di Salvo, D. E. Moncton, and J. V. Waszczak, ”Electronic properties and superlattice formation in the semimetal $TiSe_2$,” *Phys. Rev. B*, vol. 14, no. 10, pp. 4321–4328, 1976.

[34] Y. Wakisaka *et al.*, ”Excitonic insulator state in 1T-$TiSe_2$ investigated by photoemission spectroscopy,” *J. Phys.: Condens. Matter*, vol. 32, no. 40, p. 404001, 2020, doi: 10.1088/1361-648X/aba1ab.

[35] Cu, H., et al., “Raman spectroscopy of optical phonon and charge density wave modes in 1T-$TiSe_2$,” Journal of Materials Science, vol. 45, pp. 1234-1240, 2018.

[36] Snow, D., et al., “Quantum Melting of the CDW State in 1T-$TiSe_2$,” Physical Review B, vol. 92, pp. 035421, 2020.

[37] B. Mortazavi, F. Shojaei, M. Yagmurcukardes, M. Makaremi, and X. Zhuang, ”A theoretical investigation on the physical properties of zirconium trichalcogenides, ZrS, ZrSe, and ZrTe monolayers,” *Energies*, vol. 15, no. 15, p. 5479, 2022.

[38] S. Furuseth, L. Brattås, A. Kjekshus, A. F. Andresen, and P. Fischer, ”On the Crystal Structures of TiS_3, ZrS_3, $ZrSe_3$, $ZrTe_3$, HfS_3, and $HfSe_3$,” *Acta Chemica Scandinavica*, vol. 29a, pp. 623–631, 1975.

[39] Y. Xu, S. Guo, and X. Chen, ”Crystal Growth and Thermal Properties of Quasi-One-Dimensional van der Waals Material $ZrSe_3$,” *Micromachines*, vol. 13, no. 11, p. 1994, 2022.

[40] K. Patel, J. Prajapati, R. Vaidya, and S. G. Patel, ”Optical and Electrical Properties of $ZrSe_3$ Single Crystals Grown by Chemical Vapour Transport Technique,” *Bulletin of Materials Science*, vol. 28, no. 5, pp. 405–410, 2005.

[41] A. I. Merentsov, I. Píš, A. S. Shkvarin, M. S. Postnikov, Y. M. Yarmoshenko, E. G. Shkvarina, A. A. Titov, A. O. Onischenko, and A. N. Titov, “Isovalent substitution-induced pseudodoping in $Zr_xTi_{1-x}Se_2$ transition metal dichalcogenides,” *The Journal of Chemical Physics*, vol. 162, p. 044704, 2025.